

國立交通大學

電機資訊學院
光電工程研究所
碩士論文

摻雜氧化鋅奈米微晶之表面穩定強誘電性液晶元件的
分子排列與電性研究

The Study of Molecular Alignment and Electrical Properties of
Surface-Stabilized Ferroelectric Liquid Crystal with and without
Doping of ZnO Nanocrystals

研究生：李柳萱

指導教授：黃中堯 教授

中華民國九十五年六月

摻雜氧化鋅奈米微晶之表面穩定強誘電性液晶元件
的分子排列與電性研究

The Study of Molecular Alignment and Electrical Properties of
Surface-Stabilized Ferroelectric Liquid Crystal with and without
Doping of ZnO Nanocrystals

研究生：李柳萱

Student: Liu-Shiaun Li

指導教授：黃中堯

Advisors: Professor Jung Y. Huang

國立交通大學電機資訊學院

光電工程研究所

碩士論文

A Thesis Submitted to
Department of Photonics and Institute of Electro-optical Engineering
College of Electrical Engineer and Computer Science
National Chiao Tung University
in Partial Fulfillment of the Requirements
for the Degree of
Master
in
Electro-optical Engineering

June 2006
Hsinchu, Taiwan, Republic of China

中華民國九十五年六月

摻雜氧化鋅奈米微晶之表面穩定強誘電性液晶元件的 分子排列與電性研究

研究生：李柳萱

指導教授：黃中堯 教授

國立交通大學

光電工程研究所

摘要

在液晶物理的研究上及與液晶元件的發展上，時常藉著摻雜奈米結構粒子來改善液晶的分子排列與響應速度。本論文以摻雜氧化鋅奈米微晶之表面穩定強誘電性液晶(或稱鐵電相液晶)元件為研究樣本，利用影像式偏光量測系統、電容—電壓曲線、時析電光響應與時析偏振傅立葉轉換紅外光譜等量測方法，針對分子排列、光學特性、電性及外加驅動電壓下之動態響應，將摻雜氧化鋅奈米微晶之鐵電相液晶與未摻雜之鐵電相液晶相互對照。我們發現摻雜氧化鋅奈米微晶後之表面穩定鐵電相液晶，其整體液晶分子有較好的排列分布，且在無外加電場下可提升其光穿透率達 2.27 倍；此外，摻雜氧化鋅奈米晶體後之鐵電相液晶在外加相同驅動電場下，比未摻雜之強誘電性液晶元件反應速度快 2 倍。對於動態電光時析響應、二維相關光譜分析與鐵電相液晶的分子官能基排列與動態行為間的關係有深入的研究與討論。

The Study of Molecular Alignment and Electrical Properties of Surface-Stabilized Ferroelectric Liquid Crystal with and without Doping of ZnO Nanocrystals

Student : Liu-Shiaun Li

Advisors : Professor Jung Y. Huang

Department of Photonics and Institute of Electro-optical Engineering,
National Chiao Tung University

Abstract

In order to improve the electro-optical properties and response time of FLC material, doping with nanostructured materials is a newly developed technique to achieve the goal. In this thesis, we compare electrical properties and electro-optical dynamics of the surface-stabilized ferroelectric liquid crystal (SSFLC) with doping of ZnO nanocrystals (nc-ZnO) and without doping. We use several kinds of techniques, including imaging polarimetry, C-V hysteretic characterization, time-resolved electro-optical response and time-resolved FTIR, to analyze the above mentioned properties. We find that the nc-ZnO doping can improve the azimuthal and the polar alignments of FLC by reducing the full-width-and-half-maximum (FWHM) width. The approach readily improves the optical transmission property of FLC by 2.27 times at no applied field and reduces the switching time of the electro-optical response by a factor of 0.5. By using 2D IR correlation, we discovered that ZnO nanocrystals produce a novel binding effect on sub molecular fragments of FLC molecules, which lead to an improved LC alignment quality in both steady-state and dynamic processes.

誌謝

這個研究能夠順利的完成，首先要感謝我的指導教授黃中堯老師，在老師的悉心指導下，使我了解到做研究的精神是需要以嚴謹的態度及細膩的觀察來完成，雖然實驗室的人數並不多，卻也藉此讓我有更多學習的機會，最重要的是使我學會如何一個人去面對與解決問題。感謝實驗室的文慈學姊、明彰學長以及立志學長平時對我的協助，讓我在遇到問題時能夠有對象可以討論，也感謝雲漢、秉寬，跟大家一起相處、成長的日子雖然很辛苦但也真的很開心有豐碩的果實可以採收。



感謝材料所黃華宗老師提供實驗室讓我使用，感謝洪金賢學長在我遇到合成問題時不吝惜的教導我，感謝黃華宗老師實驗室所有學長姐、同學以及學弟妹對我的配合。感謝顯示所陳皇銘老師提供儀器協助我完成實驗方面的量測。感謝奇美電子以及 TTLA，在材料方面的提供。

最後要感謝我的爸媽、家人及緯仁，在我遭遇挫折時給予精神上的鼓勵與支持，希望這份成果與你們共享。

Contents

Abstract (in Chinese)	i
Abstract (in English)	ii
Acknowledgement (in Chinese)	iii
Contents	iv
List of Tables	vi
List of Figures	vii
1 Introduction	1
1.1 The overview of LC Mesophases.....	1
1.2 The overview of LC Optics.....	4
1.3 The overview of SSFLC Devices.....	6
1.4 Modification of an Existing FLC Material with Nanostructured Dopant.....	8
2 Sample Preparation and Electrical Characterization of SSFLC with and without nc-ZnO doping	10
2.1 Material Preparation and Optical Properties of nc-ZnO.....	10
2.2 Preparation of SSFLC Cells with and without nc-ZnO Doping.....	14
2.3 Alignment Quality Examination of SSFLC Cell with Imaging Polarimetry.....	17
2.4 Preisach Model and Equivalent Electronic Circuit of SSFLC Cell.....	25
2.5 Electrical Properties of SSFLC with and without nc-ZnO Doping.....	31



3	Electro-Optical Switching Dynamics of SSFLC Cells with and without nc-ZnO doping	43
3.1	Model of Electro-Optical Response of a SSFLC Cell.....	43
3.2	Time-Resolved Electro-Optical Response of SSFLC Cell.....	46
3.2.1	SSFLC cell with a driving voltage of 10V.....	46
3.2.2	SSFLC cell with a driving voltage of 5V.....	49
3.3	Time-Resolved Electro-Optical Response of SSFLC Cell with nc-ZnO Doping.....	51
3.3.1	nc-ZnO doped SSFLC cell with a driving voltage of 10V.....	51
3.3.2	nc-ZnO doped SSFLC cell with a driving voltage of 5V.....	54
4	Time-Resolved FTIR Spectroscopy of SSFLC with and without nc-ZnO Doping	57
4.1	Principle of FTIR.....	57
4.2	2D IR correlation technique.....	61
4.3	FTIR Spectroscopy of SSFLC with and without nc-ZnO doping.....	63
4.4	trFTIR of SSFLC with and without nc-ZnO doping.....	69
5	Conclusions and Future Prospect	74
	References	76

List of Tables

2-1	The fitting parameters of the pure SSFLC cell to Eq. (2-14) at different frequencies.....	36
2-2	The fitting parameters of the SSFLC cell with nc-ZnO doping to Eq. (2-14) at different frequencies.....	38
4-1	Comparison of the spontaneous polarization and viscosity of the pure FLC , FLC with ethanol residue (add a few drops of ethanol and then dried in vacuum for 8 hours, middle) and FLC doped with 1.28% nc-ZnO (add a few drops of nc-ZnO ethanol solution and then dried in vacuum for 8 hours, left).....	70



List of Figures

1-1	The molecular arrangement in the SmC, SmA, and nematic phases.....	2
1-2	Twist of the molecules in the ordinary nematic and chiral nematic phases.....	3
1-3	Twist of the molecules and the director in the SmC* phase. The chiral molecules rotate around the cone.....	4
1-4	An illustration of the LC cell inserted between a pair of crossed polarizers.....	6
1-5	The basic geometry of a bookshelf SSFLC cell structure and its electro optic switch behavior between crossed-polarizers.....	7
1-6	The two kind geometries of a chevron SSFLC cell structure applied with external electric fields.....	7
2-1	UV-visible absorption spectra of TPM-caped ZnO nanoparticles in ethanol...12	
2-2	The energy gap of the TPM-caped ZnO nanoparticle colloid was deduced from UV-visible absorption spectra in ethanol.....	13
2-3	Photoluminescence spectrum of TPM-caped ZnO nanoparticles in ethanol...13	
2-4	Schematic of an imaging polarimetric apparatus used in this study.....	17
2-5	Determination of β and d from optical intensity pattern measured on a birefringent film.....	20
2-6	The geometry of an incident optical beam on a uniaxial crystal film.....	21
2-7	The distribution of the azimuthal angle β of the SSFLC with (dash line) and without (solid line) nc-ZnO doping.....	23
2-8	The 2D distributions of the azimuthal angle β of (a) the SSFLC, (b) nc-ZnO-doped SSFLC cells.....	23
2-9	The measured images of the SSFLC test cells with and without nc-ZnO doping at five different orientations of the analyzer.....	23
2-10	The distribution of the pretilt angle $\gamma = \pi/2 - \alpha$ of the SSFLC test cells with (dashed line) and without (solid line) nc-ZnO doping.....	24
2-11	The measured images of the SSFLC with and without nc-ZnO doping at five different incident angles to deduce polar angle.....	25
2-12	The equivalent electronic circuit model of a SSFLC cell.....	26
2-13	The capacitance-voltage (C-V) curves of (a) the empty cell, (b) the cell filled with FLC at four different frequencies.....	26
2-14	The measured current-voltage (I-V) curves of the empty cell (circle-symbol) and the filled SSFLC cell (square-symbol) plotted as a function of applied voltage.....	28
2-15	Hysteresis of macroscopic polarization P(E) (top) and dielectric susceptibility $\chi(E) = \partial P / \partial E$ (bottom) for an FLC cell.....	29

2-16	The capacitance (C_{LC}) versus the applied voltage on the pure SSFLC cell without doping at four different frequencies.....	32
2-17	The capacitance (C_{LC}) versus the applied voltage on the nc-ZnO doped SSFLC cell at four different frequencies.....	33
2-18	The experimental C-V curves (open symbols) and the fitting curves (solid lines) of the SSFLC test cells without and with nc-ZnO doping cells at 100Hz.....	34
2-19	The fitting results of the measured data of (a) the SSFLC cell, and (b) the SSFLC cell with nc-ZnO doping at 100Hz. The solid lines are the fitting curve and the symbols are the measured data.....	35
2-20	The experimental C-V curves (empty symbols) and their fitting results (solid lines) of the SSFLC cells without and with nc-ZnO doping at 1 kHz.....	39
2-21	The fitting curves to Eq. (2-14) of (a) the SSFLC cell and (b) the SSFLC cell with nc-ZnO doping at 1 kHz. The symbols are the measured data.....	39
2-22	The experimental C-V curves (open symbols) and the fitting curves (solid lines) of the SSFLC cells without (square) and with (triangle) nc-ZnO doping at 10 kHz.....	40
2-23	The experimental C-V curves (open symbols) and the fitting curves (solid lines) of the SSFLC cells without (square) and with (triangle) nc-ZnO doping at 100 kHz.....	41
3-1	Schematic diagram showing the time-resolved electro-optical characterizing apparatus used in this study.....	43
3-2	Schematic diagram showing the orientational relationship between the molecular frame (ξ, η, ζ) and the sample frame (K, N, Z).....	44
3-3	Time-resolved angular pattern (symbols) of optical transmission through a SSFLC cell with 10 V at 0 μ sec and the corresponding fitting curve (solid line) to Eq. (3-4).....	46
3-4	The transient electro-optical azimuthal patterns of a SSFLC cell recorded at five different delay times. The driving field is (a) +10V, (b) -10V square waveform with a field-on duration of 800 μ s.....	47
3-5	(a) Fitting parameters (symbols) of the time-resolved EO azimuthal patterns and the applied voltage (solid line) are plotted as a function of time. (b) The deduced orientation angle of the optic axis of FLC film is shown.....	48
3-6	The normalized transient electro-optical azimuthal patterns of a SSFLC cell at four different delay times. The driving field amplitude is (a) +5V, and (b) -5V. The rubbing direction of the FLC cell is set to at 0 degree.....	49
3-7	Comparison of the fitting parameters and deduced orientation angle at two different applied voltages. The curves with circles represent the data with ± 10 V and the curves with star symbol are the data measured with ± 5 V.....	50

3-8	The normalized transient electro-optical azimuthal patterns of the pure SSFLC (square symbol) and the SSFLC with nc-ZnO doping (circle symbol) cells aligned with RN1182 were presented at no driving field amplitude.....	52
3-9	The normalized transient electro-optical azimuthal patterns of a SSFLC cell doped with nc-ZnO were presented at five different delay times. The driving field amplitude is (a) +10V, and (b) -10V.....	53
3-10	Comparing the parameters and deduced orientation angle of the optic axis of FLC film with two different cells at ± 10 V, the square symbol was SSFLC and the triangle symbol was SSFLC with nc-ZnO doping.....	54
3-11	The normalized transient electro-optical azimuthal patterns of a SSFLC with nc-ZnO doping cell are presented at four different delay times. The driving field amplitude is (a) +5V, and (b) -5V.....	55
3-12	Comparing the switching parameters and deduced orientation angle of nc-ZnO doped SSFLC cell with two different applied voltages. The curve with circle symbols is taken with ± 10 V and the lines with star symbols is with ± 5 V....	56
4-1	The excitation of a vibrational state in the electronic ground state S_0 by infrared absorption.....	57
4-2	Schematic of a FTS system.....	58
4-3	Typical setup for the asynchronous time-resolved FTIR. The signal-processing assembly for time-resolved measurement is shown on the middle, while the units constituting a conventional FTIR spectrometer are depicted in the boxes at the top and bottom.....	59
4-4	(a) FTIR spectra and (b) autocorrelation plots of the SSFLC cells with and without nc-ZnO doping at 30°C	64
4-5	FTIR spectra and (b) autocorrelation plots of the SSFLC cells with and without nc-ZnO doping in the region of 1200 to 1650 cm^{-1} measured at 30°C	65
4-6	FTIR spectra and (b) autocorrelation plots of the SSFLC cells with and without nc-ZnO doping in the region of 2800 to 3100 cm^{-1} measured at 30°C	66
4-7	FTIR angular patterns of some IR active modes at (a) 1169 cm^{-1} (b) 1250 cm^{-1} (c) 1281 cm^{-1} (d) 1391 cm^{-1} (e) 1439 cm^{-1} (f) 1514 cm^{-1} (g) 1584 cm^{-1} (h) 1608 cm^{-1} measured on the SSFLC cells with and without nc-ZnO doping at 30°C	67
4-8	FTIR angular patterns of some IR active modes at (a) 2857 cm^{-1} (b) 2931 cm^{-1} (c) 2957 cm^{-1} measured on the SSFLC cells with and without nc-ZnO doping at 30°C	68
4-9	The dynamic curve of the averaged apparent angles of IR dipoles associated with the cores of the SSFLC cells with and without nc-ZnO doping measured at 30°C . The waveform of the bipolar driving pulses is included for	

comparison.....	70
4-10 The time courses of the synchronous correlation of the C-O-C stretch mode at 1252 cm ⁻¹ of the SSFLC with and without nc-ZnO (ZnO nanocrystal solution) doping cells measured at 30°C. The waveform of the bipolar driving pulses is included for reference.....	71
4-11 Time courses of 2D IR correlation phase angle generated from the time-resolved polarization-angle dependent spectrum of (a) SSFLC and (b) SSFLC with nc-ZnO doping cells measured at 30 °C.....	73



Chapter 1

Introduction

1.1 The Overview of LC Mesophases

Liquid crystals (LC) are anisotropic fluids, with thermodynamically stable phases between the solid and the isotropic liquids. The LC phases can be classified with several kinds of sub phases with different molecular alignment orders. The typical LC molecules have the rod-like, discotic-like and the sanidic-like shapes. In this study, we focus on the rod-like molecules. The orientation of a rod-like molecule can be described by the two local axes, one parallel to the molecule noted as long axis, and the other perpendicular to it noted as short axis. Generally speaking, the LC molecules tend to align parallel to each other.

There are two main LC phases: the nematic phase and the smectic phase. The former exhibits orientation order but no positional order, while the latter reveals both orientational and partial positional order [1-3]. In the nematic phase the molecular long axes are aligned, which result in an averaged direction \mathbf{n} called the LC director. The orientation of the director represents the optic axis of the molecular thin film. The nematic phase is optical uniaxial because the two mutually independent directions perpendicular to the director are equivalent.

The smectic phase can be further divided into smectic A and smectic C as shown in the Figure 1-1. In the smectic A phase (SmA), there exists the orientational order and positional order. The molecules are oriented parallel to each other and their position is ordered in layers with the layer spacing nearly equal to the molecular

length. The director \mathbf{n} in this phase is parallel to the layer normal \mathbf{z} and determines the optic axis of the system. The SmA phase is also optical uniaxial. The Smectic C phase (SmC) possesses both orientational and positional orders. The molecules in the SmC phase are arranged in layers but not free to rotate about their long axes. The molecular long axes are tilted in a direction respected to the layer normal. The angle between the director \mathbf{n} and the layer normal \mathbf{z} is defined as the tilt angle of the material θ . The director is confined to a conical surface with the conic axis along the layer normal. The movement of the director is confined on the smectic cone. The SmC phase is optical biaxial, but it may become uniaxial under specific circumstances.

Many LC molecules usually have more than one kind of phase. Typically the phase sequence is a function of the temperature, as the following sequence: crystalline phase Cr-SmC-SmA-N-I isotropic phase (from low to high temperature).

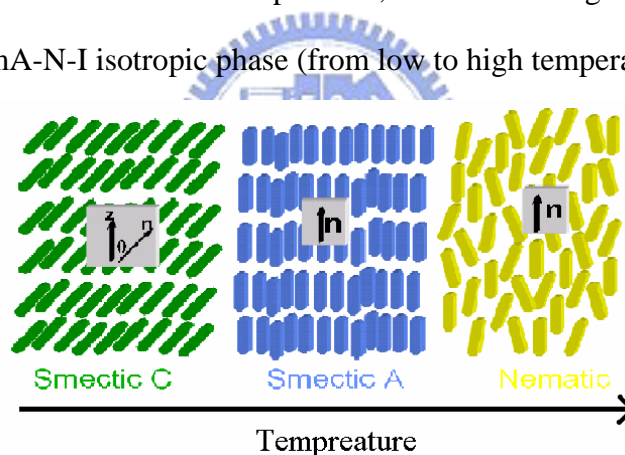


Figure 1-1 The molecular arrangement in the SmC, SmA, and nematic phases.

If the mirror symmetry elements are absent, the molecules would become chiral.

The chiral molecules and their mirror images cannot be superimposed by any translations or rotations. Doping chiral molecules into the achiral LC molecules in the nematic phase can form a so-called chiral nematic N^* phase which possess twist structure as shown in the Figure 1-2. Chiral phases are usually labeled by an asterisk “*” following the phase symbol. The director in the N^* phase, instead of being

uniformly oriented, rotates in space about an axis perpendicular to \mathbf{n} and forms a helical structure (helix). The distance, in which the director makes full 2π radians rotation along the helix axis, is called helical pitch \mathbf{p} .

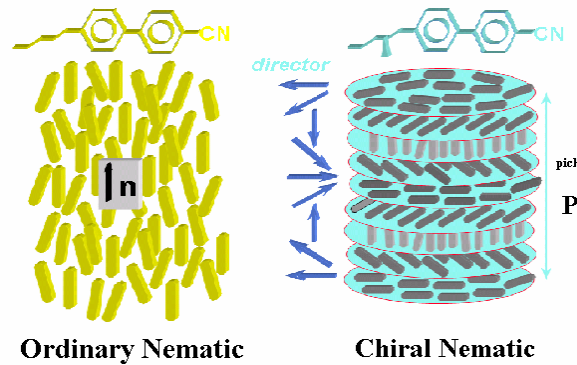


Figure 1-2 Twist of the molecules in the ordinary nematic and chiral nematic phases.

The ferroelectric SmC^* phase can be obtained either by mixing chiral molecules with achiral LC molecules in SmC phase, or by synthesizing of a molecule with a chiral part including in the molecular structure. Molecules form a helicoidal structure similarly characterized by helical pitch and its sign. A spontaneous polarization \mathbf{P}_s lying on the Smectic layer plane exhibits in the SmC^* phase. The finding of \mathbf{P}_s has been deduced from symmetry considerations [4]. In the SmC^* phase, the molecules also tilt with respect to the layer normal when the helix axis is along the layer normal which is illustrated in Figure 1-3. The director slowly rotates around the smectic cone progressively from layer to layer. Since the helical pitch is in the order of micrometers, the director rotates around the full cone over several thousands smectic layers.

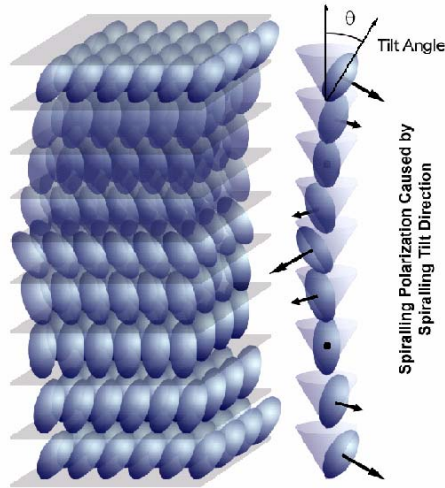


Figure 1-3 Twist of the molecules and the director in the SmC^* phase. The chiral molecules rotate around the cone.

1.2 The Overview of LC Optics

The essential properties of the LC are the optical, electric and magnetic anisotropy. Optical anisotropy means that the index of refraction of the material depends on the direction of light polarization. The LC (N or SmA) exhibits optical uniaxial symmetry with two principal refractive indices n_o and n_e . The ordinary refractive index n_o is for light with electric field polarization perpendicular to the director and the extraordinary refractive index n_e is for light with electric field polarization parallel to the director. The birefringence (optical anisotropy) is defined as $\Delta n = n_e - n_o$. If $\Delta n > 0$, the LC is said to be optically positive whereas if $\Delta n < 0$, the LC is said to be optically negative. The biaxial material (SmC) exhibiting two optic axes can be characterized by three principle refractive indices: n_1 , n_2 and n_3 . The difference $\delta n = n_2 - n_1$ is called optical biaxiality. Since the biaxiality of LC is very small ($n_1 \sim n_2$) and can be neglected in most cases [5]. A light beam entering the LC layer is split to two components: the ordinary and extraordinary rays which are so-called n_o and n_e . Both rays propagate through the birefringent medium at different

velocities and then cause a phase retardance Γ at the output of a uniformly aligned LC layer. The phase difference is defined as:

$$\Gamma = \frac{2\pi}{\lambda} \Delta n \cdot d \quad (1.1)$$

where λ is the wavelength of light in vacuum and d is the distance across the homogeneous LC layer which is equal to the cell gap as normal incidence. The optical transmission through a LC layer can be determined by the Jones matrix method. Assuming that the LC layer is inserted between a pair of crossed polarizers shown in the Figure 1-4, where the transmission axis of the polarizer is along the x-axis and the analyzer is along the y-axis, the angle between the polarizer and the optic axis of LC cell is θ , the resulting optical transmission can be calculated as:

$$E = \begin{pmatrix} 0 & 0 \\ 0 & 1 \end{pmatrix} \begin{pmatrix} \cos \theta & -\sin \theta \\ \sin \theta & \cos \theta \end{pmatrix} \begin{pmatrix} e^{\frac{\Gamma}{2}} & 0 \\ 0 & e^{-\frac{\Gamma}{2}} \end{pmatrix} \begin{pmatrix} \cos \theta & \sin \theta \\ -\sin \theta & \cos \theta \end{pmatrix} \begin{pmatrix} 1 & 0 \\ 0 & 0 \end{pmatrix} E_0 \quad (1.2)$$

where E_0 is the electric vector of the input linearly polarized beam, E is that of the optical field exiting from the analyzer, and Γ is the phase difference induced by LC cell. The transmitted intensity can then be written as:

$$I = E^* \cdot E = I_0 \sin^2 2\theta \sin^2 \frac{\Gamma}{2} \quad (1.3)$$

where I_0 is the intensity of the linearly polarized light. In this case with the 2×2 Jones matrix, we neglect the reflections and the interference effects of light. The more accurate solution can be derived by using 4×4 propagation matrix approaches, which can take into account the above-mentioned effects.

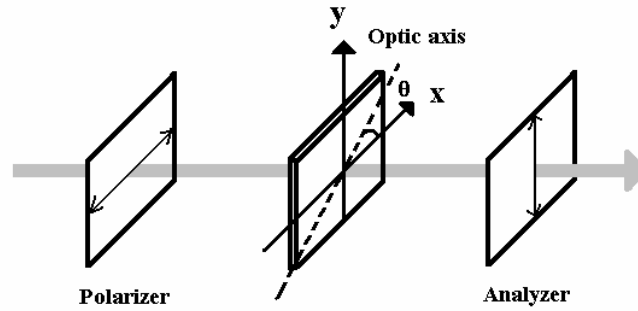


Figure 1-4 An illustration of the LC cell inserted between a pair of crossed polarizers.

1.3 The Overview of SSFLC Devices

Surface-stabilized ferroelectric liquid crystal (SSFLC) device, which was first proposed by Clark and Lagerwall in 1980, had attracted significant interest. SSFLC can provide attractive features of microseconds response, bistability, and wide viewing angle [6, 7]. SSFLC uses a very thin cell with cell gap slightly smaller than the helical pitch to unwind the helical structure of LC. The cell gaps generally are of the order of couples micrometers. The simplest geometry of bookshelf SSFLC cell structure is shown in the Figure 1-5. Besides the bookshelf structure, geometry is chevron structure, in which the internal layers are folded as shown in the Figure 1-6.

Assuming that the FLC molecules are sandwiched between two bounding plates and the smectic layers are normal to the plates. The boundary forces on the surface of the plates align \mathbf{n} to lie on the plane. The boundary-induced preferred orientation, and the constraint of FLC which demands \mathbf{n} on the tilt cone, result in two possible orientations of \mathbf{n} at the intersections of the tilt cone with the surface of bounding plates. The spontaneous polarization \mathbf{P}_s can adopt only down or up orientation (see Figure1-5). This leads to the appearance of spontaneous domain of uniform polarization, which renders this structure to be ferroelectric. In an ideal case there are two \mathbf{n} orientations, which are symmetric with equal minimum free energy. When an electric field is applied along the surface normal, the spontaneous polarization will

align itself in the direction of the external field. Any deviation from these two directions produces a torque $\Gamma_f = P \times E$. Because the spontaneous polarization is coupled to the director it will drag the director on the smectic cone to the other extreme state. When the field is turned off, the current state will be maintained. The FLC cannot switch when the applied field is lower than the threshold field. These properties result in a hysteretic behavior, which makes FLC very useful for a passive-matrix device.

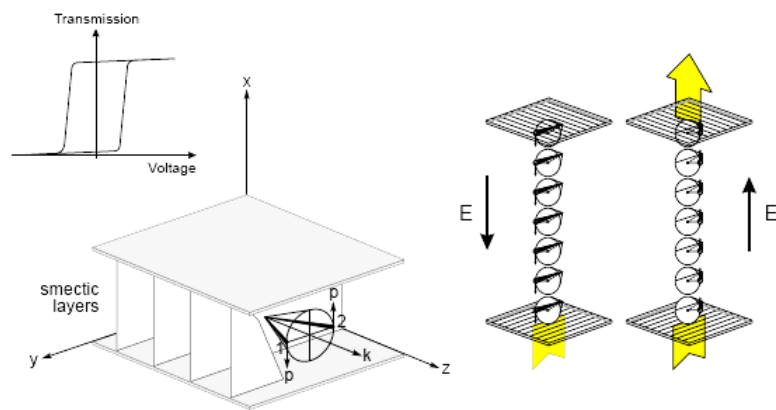


Figure 1-5 The basic geometry of a bookshelf SSFLC cell structure and its electro optic switch behavior between crossed-polarizers.

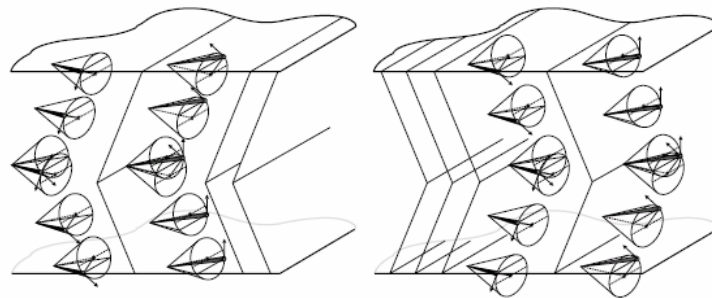


Figure 1-6 The two kind geometries of a chevron SSFLC cell structure applied with external electric fields.

1.4 Modification of an Existing FLC Material with Nanostructured Dopant

Modifications of the electro-optical properties of an existing FLC material by doping with appropriate impurities had recently attracted significant interest. Concerted efforts in nanostructured materials and LC technologies had been employed to demonstrate the potential to yield an improved LC alignment and EO properties. The developments had also revealed that the phase transition, elastic coupling, ionic effect, and dielectric anisotropy of LC materials are adjustable with doping of various nanomaterials, such as silica particles, LC-covered Pd particles, and ferroelectric nanoparticles, *etc.* The design parameters of the methodology include material, size and shape, doping concentration and surfactant properties of nanoparticles, which could open an effective and flexible way for generating promising new materials for the next generation LC flat panel display.

Recently, Zinc oxide (ZnO) nanostructured materials had been widely studied for the potential applications with its optical, electrical and mechanical properties. Experimental and theoretical studies on ZnO crystals have revealed a presence of giant permanent dipole moment, which yield a significant piezoelectric effect, and therefore ZnO has been considered to be promising for micromechanical devices. Zinc oxide is a wide direct band-gap (3.4 eV) II-VI semiconductor with wurtzite structure and large exciton binding energy (60 meV). Therefore it has also been used in short wavelength electro-optical devices such as light emitting diodes and lasers. From the viewpoint of material synthesis, ZnO crystals offer further advantages of low cost and poison-free preparation procedure compared with other popular nano objects such as CdS, CdSe, and InP, *etc.*

Since development of a new FLC material with attractive properties is an extremely time consuming effort, modification of an existing material to fit into a

specific application becomes an attractive tactic. In this thesis, we explore the possibility to enhance application properties of a FLC material by doping the FLC with ZnO nanoparticles. To our knowledge, modification of the electro-optical properties of a smectic liquid crystal with semiconductor nanocrystals has not yet been reported.



Chapter 2

Sample Preparation and Electrical Characterization of SSFLC with and without nc-ZnO Doping

2.1 Material Preparation and Optical Properties of nc-ZnO

Colloidal ZnO nanoparticles with an average diameter of 3.2 nm were prepared by following the procedure described in previous reports [8]. In a typical run, 3.29 g of zinc acetate dihydrate ($\text{Zn}(\text{Ac})_2 \cdot \text{H}_2\text{O}$) (SHOWA, 99.0%) was dissolved in 150 ml boiling ethanol (Nasa, 99.5%) and refluxed the solution at about 80°C in a nitrogen atmosphere. The solution was held at 80°C for 3 hours with vigorous stirring. After this process, 90 ml of ethanol was removed from the solution by distillation and subsequently the same amount of fresh ethanol was added to the original volume. Then the solution was cooled to 0°C.

0.87 g lithium hydroxide monohydrate ($\text{LiOH} \cdot \text{H}_2\text{O}$) (TEDIA, 99.0%) was added into 90 ml ethanol under constant stirring for 2 hours. When needed, sonication was used to ensure complete dissolution of $\text{LiOH} \cdot \text{H}_2\text{O}$ in ethanol. Afterwards, the resulting ethanol solution of $\text{LiOH} \cdot \text{H}_2\text{O}$ was added drop-by-drop into the above-mentioned zinc acetate solution which had been cooled to 0°C and was under constant stirring. The solution was warmed up to room temperature and continuously stirred for 2 hours until a transparent colloid solution of ZnO nanoparticles was formed.

To stabilize the ZnO nanoparticles, 0.3-g 3-(Trimethoxysilyl) propyl methacrylate (TPM) (Aldrich, 98.0%) was dissolved in 10 ml ethanol and then this solution was slowly injected into 240-ml as-prepared colloid solution of ZnO

nanoparticle over about 1 hour at 0°C. The mixture was stirred at room temperature for 12 hours followed by filtration with a 0.45-μm glass fiber filter to remove any insoluble precipitates [9].

To purify nc-ZnO colloid solution and then collect ZnO nanopowder, the nc-ZnO colloid was precipitated by adding an excess of hexane or heptane into the ethanol solution with a volume ratio of heptane/ethanol >2 [10]. In a typical run, 20 ml colloid solution of ZnO nanoparticles was slowly poured into 60 ml heptane (Nasa, 96%) to produce nc-ZnO precipitation. The resulting precipitation was isolated by centrifugation. Dissolve the above precipitate in ethanol and rewash the solution with heptane several times to remove all residues. To obtain ZnO nanopowder, the final precipitate was isolated with centrifugation and dried by purging with pre-purified nitrogen gas.

UV-visible absorption spectra were measured with an Agilent 8453 UV-Visible Spectroscopy using a 1-cm quartz cuvette at room temperature. The TPM-modified ZnO nanoparticle solution was diluted with fresh ethanol to appropriate optical density. Typical UV-Vis absorption spectrum of the ZnO nanoparticle solution is shown in Figure 2-1. The absorption peak and the shoulder ($\lambda_{1/2}$) of the ZnO nanoparticle colloids were found to locate at 327 nm and 345.6 nm, respectively. The UV-Visible absorption spectrum is useful to characterize the particle growth process because the absorption is closely associated with particle size [10-12]. According to the experimental result reported by Meulenkamp [10], the particle sizes can be estimated from the measured $\lambda_{1/2}$ by

$$\frac{1240}{\lambda_{1/2}} = 3.301 + \frac{294.0}{D^2} + \frac{1.09}{D} \quad (2.1)$$

Based on the equation, we estimate that the diameter of our TPM-caped ZnO nanoparticles is about 3.4 nm.

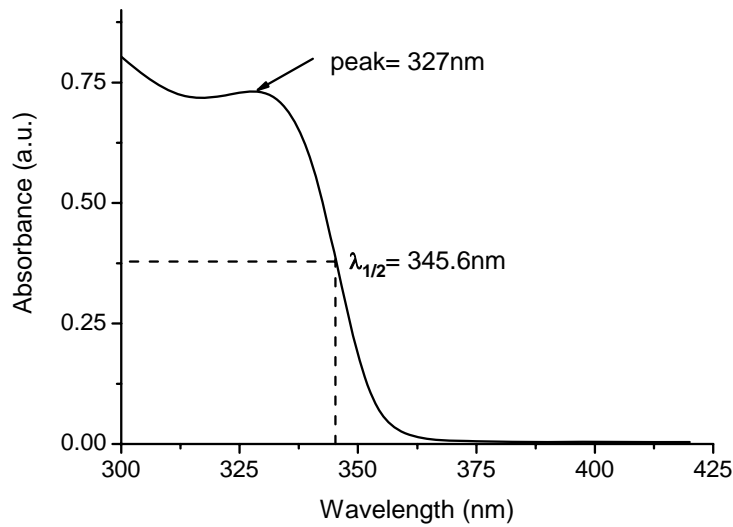


Figure 2-1 UV-visible absorption spectra of TPM-caped ZnO nanoparticles in ethanol.

The bandgap of the TPM-caped ZnO nanoparticles can also be determined from the UV-Visible absorption spectrum [11, 12]. The transmitted and incident light intensities I_t and I_0 are related via the Beer's law $I_t = I_0 \exp(-\alpha L)$, where α is the absorption coefficient and L the optical path length of the sample. ZnO is a direct-bandgap semiconductor with an absorption coefficient α relating to the optical excitation energy $h\nu$ by $\alpha = A(h\nu - E_g)^{1/2}$ (for $h\nu \geq E_g$), where E_g is the fundamental energy bandgap. Therefore, to retrieve the bandgap energy we plot $[\ln(I_t/I_0)]^2$ versus optical energy $h\nu$. Extrapolating the linear part until it intersects the x-axis, which yields E_g . Based on this method, the bandgap of the TPM-caped ZnO nanoparticle colloid was found to be about 3.54 eV, as shown in Figure 2-2.

Similar to the UV-Vis absorption spectrum, photoluminescence spectrum of nc-ZnO colloid is also sensitive to the preparation procedure [12]. The photoluminescence properties of nc-ZnO solution were investigated with Hitachi F4500 Fluorescence Spectrometer. The sample is contained in a 1-cm quartz cuvette

and excited by an optical beam with wavelength of 300 nm at room temperature. The photoluminescence spectrum of the TPM-caped colloidal ZnO nanoparticles with an averaged diameter of 3.4 nm is presented in Figure 2-3. The fluorescence from our TPM-caped nc-ZnO colloidal solution exhibits a green emission peak at 518 nm.

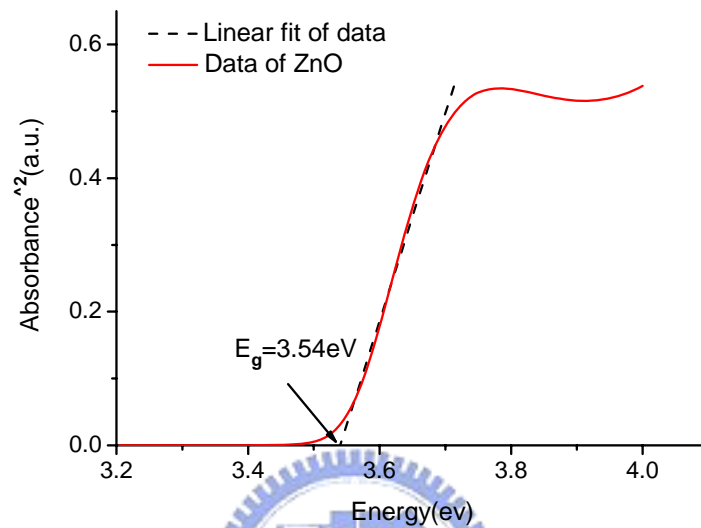


Figure 2-2 The energy gap of the TPM-caped ZnO nanoparticle colloid was deduced from UV-visible absorption spectra in ethanol.

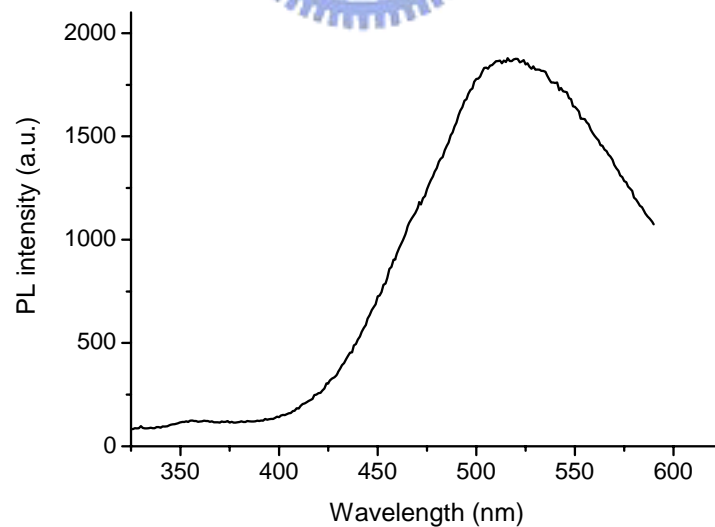


Figure 2-3 Photoluminescence spectrum of TPM-caped ZnO nanoparticles in ethanol.

2.2 Preparation of SSFLC Cells with and without nc-ZnO Doping

The surface-stabilized ferroelectric liquid crystal samples used in this study were prepared with a procedure to be detailed in this section.

1. Substrate Cleaning: Two kinds of substrates were used to prepare SSFLC test cells. The ITO-coated fused silica substrates were used for optical measurements in the spectral range from UV to visible. For IR spectroscopic studies, we select ITO-coated CaF₂ substrates. The substrates were cleaned with the following steps:

1. Soak the substrates in a diluted detergent aqueous solution for 15 min.
2. Wash the soaked substrates with the diluted detergent solution, then rinse with deionized (DI) water.
3. Put the washed substrates in a fresh detergent aqueous solution and ultrasonic treatment for 15 min.
4. Rinse every substrate with DI water, and then ultrasonic the substrates in clean DI water for 5 min.
5. Repeat the step 4.
6. Put as treated substrates into acetone and ultrasonic vibration treatment for 15 min.
7. Rinse the substrates with clean DI water. Put them into a fresh DI water bath to perform ultrasonic vibration treatment for 15 min. Repeat the step for two times.
8. Rinse the substrates with DI water and purge with nitrogen gas to dry the substrates.
9. Put the substrates into clean oven to bake at 100°C for 1hr.

2. Preparation of LC Alignment Layer: The selection of alignment material depends on the desired parameters of LC test cell such as pretilt angle, anchoring

energy, and residue charge on the surface of alignment layer. In this thesis study, a polyimide RN1182 from Nissan Chemical was used. We applied a rubbing process to produce the easy axis for LC alignment on RN1182-coated ITO substrates. The preparations of alignment layers are described in the following:

1. Wait for the temperature of RN1182 and its diluting solvent to warm up to room temperature. Dilute the RN1182 with the solvent to a concentration of 25% in weight.
2. Stir the diluted RN1182 solution for 2 hours at room temperature.
3. Put droplets of diluted solution of RN1182 on substrate surface. The amount of the solution deposited depends on the size of substrate.
4. Spread the alignment layer on the substrate with a spin coater. The spinning rate should be optimized based on the viscosity of the spreading solution. The spinning rate used for RN1182 is 300 rpm for 10 sec and then 3000 rpm for another 30 sec.
5. Soft bake the coated substrates in an oven at 80°C for 5 min after the spin coating procedure is completed.
6. Hard bake the coated substrates at 250°C for another 60 min.
7. Rub the coated substrates with a rubbing machine. The distance between the roller and the substrate is about 0.5 mm. Set the rotation speed of the roller at 1000 rpm and the translation speed of the substrates about 5 cm/min. Check the rotation direction of the roller to ensure sufficient relative velocity existing between roller and substrate.

3. FLC Preparation: To prepare FLC with an appropriate doping of nc-ZnO, the ferroelectric liquid crystal material FELIX -017/100 mixture from Clariant was used. The phase transition sequences are I-N at 86°C-83°C, N-S_A at 77°C, S_A- S_C at 73°C, S_C-X at -28°C. Two different procedures were used in order to find out the best

preparation approach of nc-ZnO-doped FLC:

A. Mix nc-ZnO Powder with FLC

1. Take a suitable amount of pure FLC, and then add several milligrams of nc-ZnO powder to the desired weight percentage. In this study, FELIX -017/100 doped with nc-ZnO powder to a weight percentage of 1.06% was used.
2. Put the mixture into an ultrasonic water bath at about 85°C to keep the FLC in the isotropic phase and performed ultrasonic treatment for 40 min.
3. Put the mixture in vacuum and wait for its temperature return to room temperature.

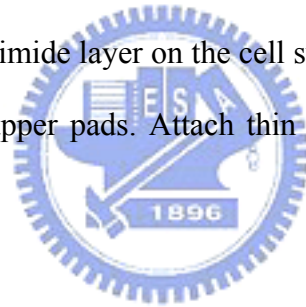
B. Mix FLC with nc-ZnO Ethanol Solution

1. Take an appropriate amount of pure FLC. Add several milligrams of TPM-caped nc-ZnO ethanol solution (what is the concentration of nc-ZnO in the ethanol solution) to a desired weight percentage. In this study, FLC FELIX -017/100 doped with nc-ZnO to a weight percentage of 1.086% was used.
2. Put the mixture into an ultrasonic water bath at about 85°C to keep the FLC in the isotropic phase and performed ultrasonic treatment for 5 min. Wait for the mixture returns to room temperature.
3. Put the mixture in vacuum line and purge it with nitrogen gas for 8 hours to drive the remaining ethanol out of the mixture.

4. Test Cell Assembly: The gap of the test cells used is controlled by silica balls with a diameter of 2 μm . The assembly of a test cell and liquid crystal filling are described as follows:

1. The silica balls were dispersed into a UV-curable gel NOA65 with a volume fraction of silica balls about 5% in the mixture.

2. Coat the spacer solution along the two parallel rims of one substrate.
3. Assemble the substrates into a test cell with a desired rubbing geometry. Adjust the cell gap to achieve the best gap uniformity.
4. Cure the UV gel by exposing the test cell with UV light.
5. Put the empty cell on a hot plate with a temperature of 87°C to keep the FLC used in the isotropic phase.
6. Put several droplets of FLC (or FLC doped with nc-ZnO) on the opening side of the empty test cell. Wait the test cell filled with FLC (nc-ZnO doped FLC) via capillary force.
7. Cool down the filled cell to room temperature slowly and then seal the opening sides of the cell with a quick-dry sealant.
8. Carefully remove the polyimide layer on the cell substrates to expose the ITO film and put on conducting copper pads. Attach thin copper wires to the conducting copper pads.



2.3 Alignment Quality Examination of SSFLC Cell with Imaging Polarimetry

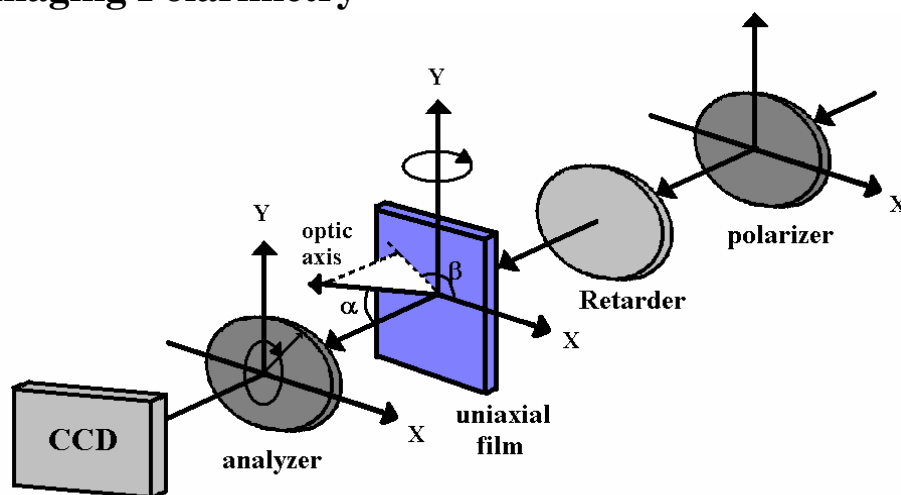


Figure 2-4 Schematic of an imaging polarimetric apparatus used in this study

Figure 2-4 presents a schematic diagram of the imaging polarimetric system used for probing the alignment quality of a SSFLC cell [13]. The polarimetric setup includes a polarizer, a retarder, a test sample, an analyzer, and an image detector. The FLC test cell, which is assumed to be a homogeneous uniaxial film, was mounted on a rotation stage to allow an accurate orientation adjustment. The light source was a laser diode with a wavelength of 670 nm. The light beam was expanded with a 40-times beam expander to yield a region with a uniform intensity distribution. The beam was transformed into a right-hand circularly polarized light with a polarizer and a variable retarder. After the right-hand circularly polarized light passes through the test cell, the polarization state of the transmitting light was analyzed with a polarization analyzer and then was imaged onto a 2D charge-coupled device (CCD). The sample plane was defined to be x-y plane, and the polar angle of the optic axis of the sample was defined to be α from the z-axis. The optic axis was projected onto the x-y plane to yield an azimuthal angle β relative to the x-axis.

The 2D CCD detector has an imaging area of $7 \times 5 \text{ mm}^2$ with pixel arrays of $426(H) \times 320(V)$. The 2D intensity data measured by the CCD camera was transformed into National Television System Committee (NTSC) signal and sent to a computer, which contained an image processing circuit board. The image processing board had picture elements of $640(H) \times 480(V)$ with 8-bit coding for each pixel. To reduce the memory storage, we render nine- (3×3) -elements array into one element to form an image with a smaller size of 34,000 elements. We used Matlab as our image processing platform.

By using Jones calculus, we can derive an expression for the optical irradiance on each pixel of CCD detector [14] :

$$\begin{bmatrix} E'_x \\ E'_y \end{bmatrix} = J_{PSA} J_f J_{PSG} E_{in} = E_0 \begin{bmatrix} \cos^2 \phi & \sin \phi \cos \phi \\ \sin \phi \cos \phi & \sin^2 \phi \end{bmatrix} \begin{bmatrix} \xi & \eta \\ \eta & \varsigma \end{bmatrix} \frac{1}{\sqrt{2}} \begin{bmatrix} 1 & i \\ i & 1 \end{bmatrix} \begin{bmatrix} 1 \\ 0 \end{bmatrix} \quad (2.2)$$

The Jones matrix elements (J_f) of a uniaxial film can be written as [15]:

$$\begin{aligned}\xi &= \cos^2 \beta e^{i\delta/2} + \sin^2 \beta e^{-i\delta/2}, \\ \eta &= i \cos^2 \beta e^{i\delta/2} + \sin^2 \beta e^{-i\delta/2} \\ \zeta &= \cos^2 \beta e^{-i\delta/2} + \sin^2 \beta e^{i\delta/2}\end{aligned}\quad (2.3)$$

The retardance of the transmitted light will experience an optical retardance of

$$\delta(\alpha) = \left(\frac{2\pi}{\lambda} \right) h \left(\frac{1}{\sqrt{\frac{1}{n_e^2} \sin^2 \alpha + \frac{1}{n_o^2} \cos^2 \alpha}} - n_o \right), \quad (2.4)$$

where h denotes the film thickness. Here we assume that the index of refraction of the film to be uniform over the entire film thickness, and the indices are known a priori.

By using Eq. (2.2), the optical intensity on the detector can be expressed as

$$I = E'_x E'_x{}^* + E'_y E'_y{}^* = \frac{I_0}{2} \{1 + \sin 2(\phi - \beta) \sin \delta\}, \quad (2.5)$$

where I_0 denoted the incident beam intensity, and ϕ is the azimuthal angle of the polarization state analyzer (PSA).

The Measurement Principle of the Azimuthal Angle (β)

Notice that $\sin(\delta)$ is a constant because retardation is a function of polar angle and sample thickness, which were kept constant during the measurement (see Eq. (2.2)). Therefore we can determine the azimuthal angle β of the optic axis by fitting the measured intensity pattern $I(\phi)$ at normal incidence to Eq. (2.5) with $\sin(\delta)$ and β as the fitting parameters. The angle ϕ is typically rotated from 0° to 180° and every 10° we record the intensity distribution with the CCD. That results in a 19-points intensity curve for each pixel, and can be fitted to Eq. (2.5) to retrieve β at each pixel with the nonlinear least-squares method.

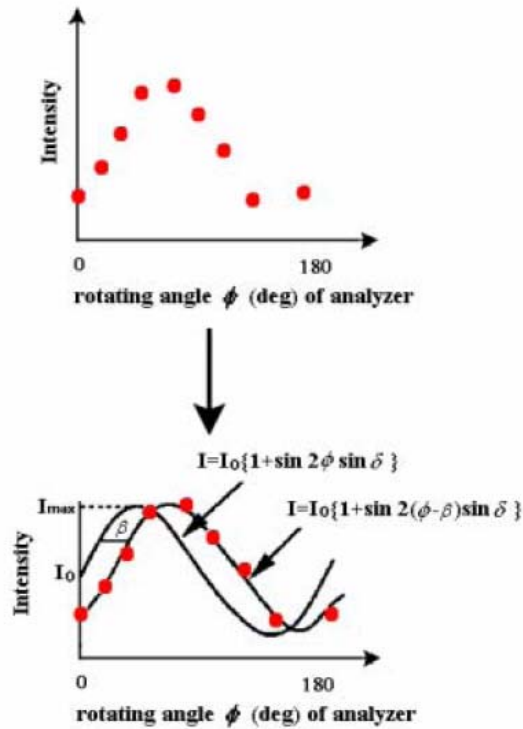
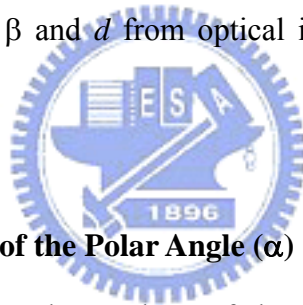


Figure 2-5 Determination of β and d from optical intensity pattern measured on a birefringent film.



The Measurement Principle of the Polar Angle (α)

After β was determined, polar angle α of the optic axis and thickness of the sample can be determined by rotating sample along the z-axis with ϕ adjusting to meet $\sin[2(\phi-\beta)]=1$ (*i.e.*, $\phi-\beta=\pi/4$). We changed the incident angle by rotating the sample about y-axis. The incident angle between the incident light and sample normal was denoted by ψ , as shown in Figure 2-6.

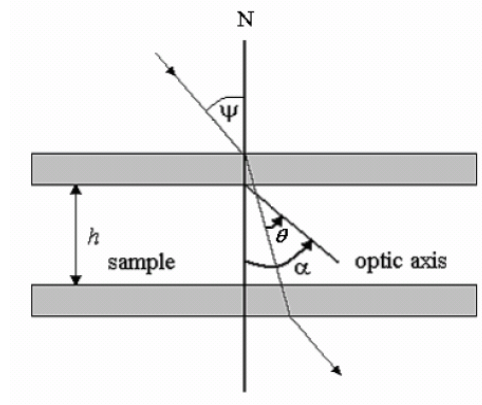


Figure 2-6 The geometry of an incident optical beam on a uniaxial crystal film.

When an obliquely incident light passed through the sample, the optical retardation experienced can be expressed as

$$\delta(\gamma, \psi) = \frac{2\pi}{\lambda} \cdot h \cdot f(\gamma, \psi) \quad (2.6)$$

where $\gamma \equiv \pi/2 - \alpha$, and $f(\gamma, \psi)$ was shown to be [16]:

$$f(\gamma, \psi) = \frac{1}{c^2} (a^2 - b^2) \sin \gamma \cos \gamma \sin \psi + \frac{1}{c} \left(1 - \frac{a^2 b^2}{c^2} \sin^2 \psi\right)^{1/2} - \frac{1}{b} (1 - b^2 \sin^2 \psi)^{1/2}, \quad (2.7)$$

$$a = \frac{1}{n_e}, b = \frac{1}{n_o}, c = a^2 \cos^2 \gamma + b^2 \sin^2 \gamma$$

where n_e and n_o denote the refractive indexes of the extraordinary and the ordinary waves in the uniaxial film. We first noticed that when the polar angle α is fixed (γ is therefore fixed), we can rewrite the optical transmittance as

$$T(\psi) = \frac{1}{2} [1 + \sin \delta(\psi)]. \quad (2.8)$$

Eq. (2.8) indicates that the optical transmittance varies with the incident angle and the variation pattern depends on the polar angle α of the optic axis and the thickness h of the uniaxial film. Therefore, we can fit the measured curves to Eq. (2.8) to retrieve the 2D distributions of α and h .

Distribution of the Azimuthal Angle β of SSFLC Film with and without nc-ZnO Doping

In this study, we prepared nc-ZnO doped SSFLC by direct mixing the nc-ZnO powder into FLC. The 2D distributions of the azimuthal angle of SSFLC cells with and without nc-ZnO doping are presented in the Figure 2-7. We found the distribution of the azimuthal angle of the pure FELIX -017/100 SSFLC cell peaks at 9° (the x-axis set to be 0°) with a FWHM of 16° . However, the distribution of SSFLC with nc-ZnO doping peaks at 17° with a FWHM of 13° . We should point out that azimuthal distribution of LC director directly reflects the optical properties of the LC device. Thus, clearly nc-ZnO doping improves the azimuthal alignment and results in a narrower distribution.

The 2D distribution images of the azimuthal angle of the two SSFLC test cells were shown in Figure 2-8 with an image size of 50×50 pixels. The color code indicates the magnitude of the azimuthal angle and the black short lines represent the liquid crystal directors projected on the substrate surface. For comparisons, the measured image patterns of the two test cells under different analyzer orientations are presented in Figure 2-9. It is observed that the similar streaks of these two test cells reveal in both measured image patterns and 2D distributions of the azimuthal angle. The variation of SSFLC from dark to bright are more obvious than that of nc-ZnO doped SSFLC in the same angle range. This difference make the SSFLC has higher distributing numbers than nc-ZnO doped SSFLC at the statistic of the azimuthal angle. However, the nc-ZnO doped SSFLC cell yields a darker image, indicating a narrower azimuthal distribution. The streaks of the SSFLC with nc-ZnO doping cell are not such apparent as that of the SSFLC cell, hence the entire 2D distributions of the azimuthal angle of nc-ZnO doped is more uniform.

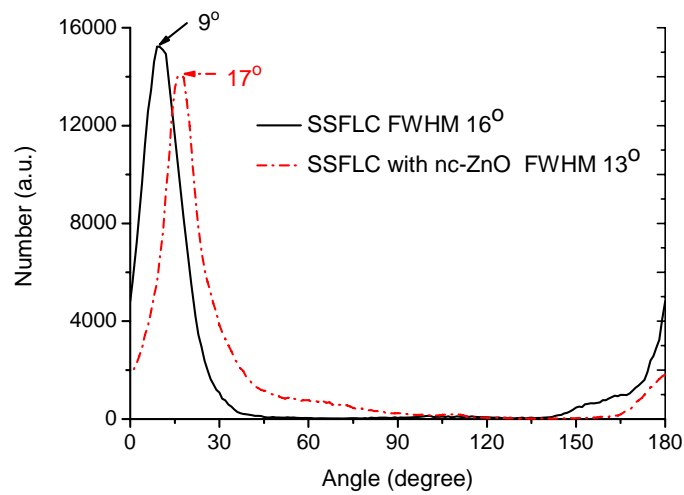


Figure 2-7 The distribution of the azimuthal angle β of the SSFLC with (dash line) and without (solid line) nc-ZnO doping.

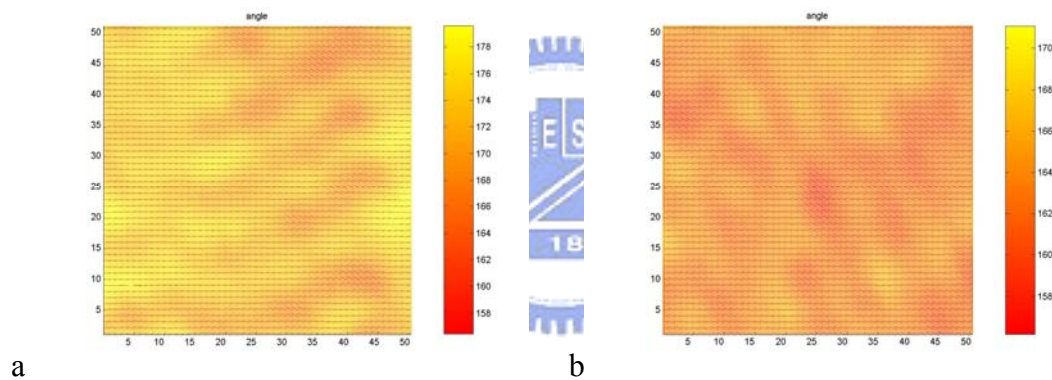


Figure 2-8 The 2D distributions of the azimuthal angle β of (a) the SSFLC, (b) nc-ZnO-doped SSFLC cells.

	0°	40°	90°	130°	170°
SSFLC					
SSFLC with nc-ZnO doping					

Figure 2-9 The measured images of the SSFLC test cells with and without nc-ZnO doping at five different orientations of the analyzer. These images are part of the data,

which were used to retrieve the 2D distribution of azimuthal angle shown in Figure 2-8.

Distribution of the Polar Angle α of SSFLC Film with and without nc-ZnO Doping

The 2D distributions of the polar angle of SSFLC test cells with and without nc-ZnO doping are presented in Figure 2-10.

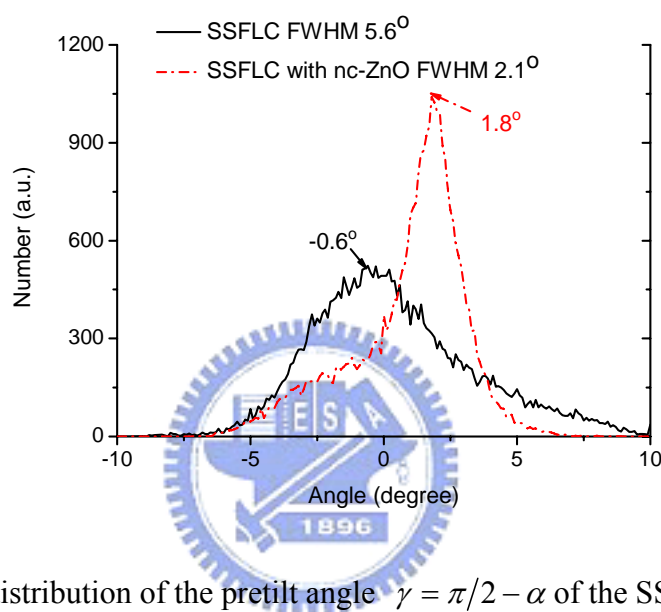


Figure 2-10 The distribution of the pretilt angle $\gamma = \pi/2 - \alpha$ of the SSFLC test cells with (dashed line) and without (solid line) nc-ZnO doping.

The distribution of the pretilt angle of pure FELIX -017/100 test cell was found to peak at -0.6° (the z-axis set as 90°) with a FWHM of 5.6° . The doping of nc-ZnO into FELIX -017/100 leads to a distribution peak at 1.8° with a FWHM of 2.1° . We found that the nc-ZnO doping also improves the polar distribution of FLC director by effectively reducing the FWHM width. This improvement may originate from a novel effect of nc-ZnO to effectively tie surrounding FLC molecules together with its giant dipole moment.

To give clearer comparisons of the transmitting light intensity variation, the measured images of the SSFLC test cells without and with nc-ZnO doping were

collected and shown in Figure 2-11 at five different incident angles. Here 0° denotes that the incident light was normal to the test cell. These images are part of the data, which were used to retrieve the 2D distribution of azimuthal angle shown in Figure 2-10. The nc-ZnO doped SSFLC cell yields a darker image and the streaks of it are also less than the SSFLC cell, indicating a narrower pretilt distribution. Besides, it presents an asymmetric phenomenon to produce the pretilt distribution shift 1.8 degrees.




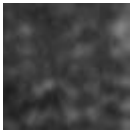





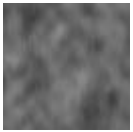
	-40°	-20°	0°	20°	40°
SSFLC					
SSFLC with nc-ZnO doping					

Figure 2-11 The measured images of the SSFLC with and without nc-ZnO doping at five different incident angles to deduce polar angle.

2.4 Preisach Model and the Equivalent Electronic Circuit of SSFLC Cell

Equivalent Electronic Circuit Model

To accelerate the applications of a FLC device, many papers have been published to propose an equivalent electronic circuit model for FLC cell in DHF-LCDs and TLAFLCDs [17-19]. The electronic model can help us analyzing the dynamic behavior of the FLC molecules with an external electric field. In this study, we develop an equivalent electronic circuit model of SSFLC cells to reveal more clearly the effect of the nc-ZnO doping.

The resulting effective circuit model is presented in Figure 2-12. Here C_p and R_p

denote the capacitance and resistance of the polymer alignment layer, and C_{LC} and R_{LC} reflect the dynamic capacitance and resistance of the FLC layer. The total capacitance of the SSFLC cell C_{cell} can be determined from electrical measurement. The electrical characterization apparatus used in this study was a HP4284A LCR meter. The characterization procedure starts with a careful measurement of the total capacitance of the empty cell at four different frequencies. The results are presented in Figure 2-13(a), which exhibits that the capacitance decreases with an increase of frequency. At a fixed frequency, the capacitance is nearly constant independent of the applied voltage.

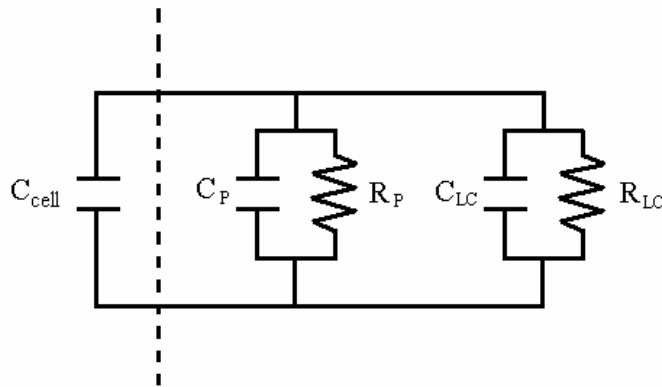
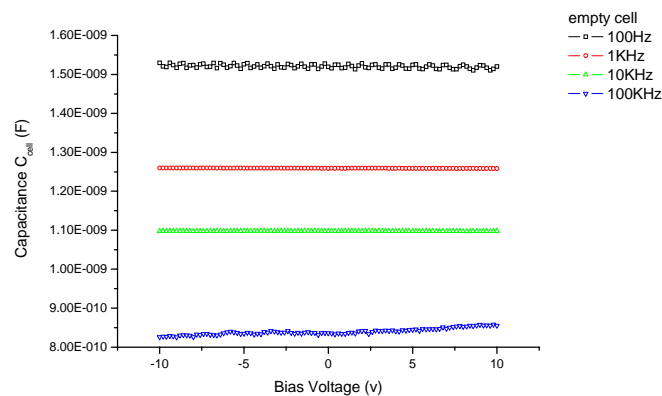


Figure 2-12 The equivalent electronic circuit model of a SSFLC cell

a. The empty cell



b. The SSFLC cell

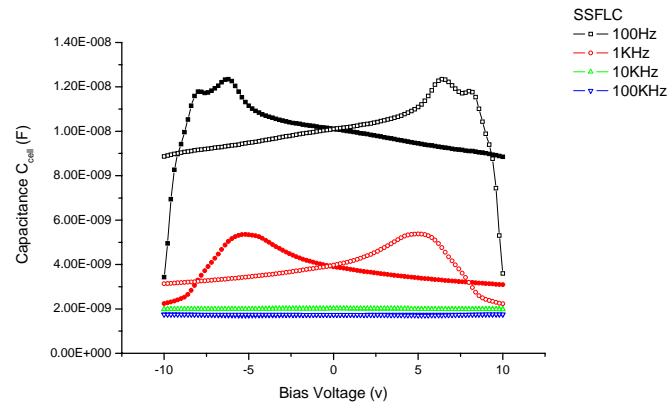


Figure 2-13 The capacitance-voltage (C-V) curves of (a) the empty cell, (b) the cell filled with FLC at four different frequencies.

We can therefore determine the capacitance of the ITO/polymer alignment layer directly and from the result we also can deduce the current-voltage curve of the empty cell. The result is presented in Figure 2-14. The measurement result suggests that the capacitance and resistance of the ITO/polymer layer should be connected in a parallel form in the electronic circuit.

We filled the test cell with FLC and measured its C-V curve again. We found that the total capacitance of the cell becomes a function of the applied voltage, as shown in Figure 2-13(b). The capacitance of the filled cell was larger than that of the empty cell at about 1-2 order. The C-V curve profiles also change with frequency. According to the result, we connect the capacitances of the FLC layer and the polymer layer in parallel. The current-voltage curve (I-V) of the SSFLC cell measured with a DC voltage was shown in Figure 2-14. Comparing with the empty cell, the current flowing through the SSFLC cell is increased. This meant that the resistance of the SSFLC was smaller than that of empty cell deduced from the Ohm's law. From this IV result, we conclude that the resistances of the polymer layer and the FLC layer should be connected in a parallel form.

The charge stored in a SSFLC cell can be expressed as

$$C_{cell} \cdot V_{ext} = \int^{V_{ext}} C_p \cdot dV + \int^{V_{ext}} C_{LC} \cdot dV \quad (2-9)$$

The resulting equivalent electronic circuit model of SSFLC shown in Figure 2-12 can be used to describe the variation of the capacitance of the FLC layer with applied voltage. The same approach can be applied to analyze the behavior of the SSFLC cell with nc-ZnO doping.

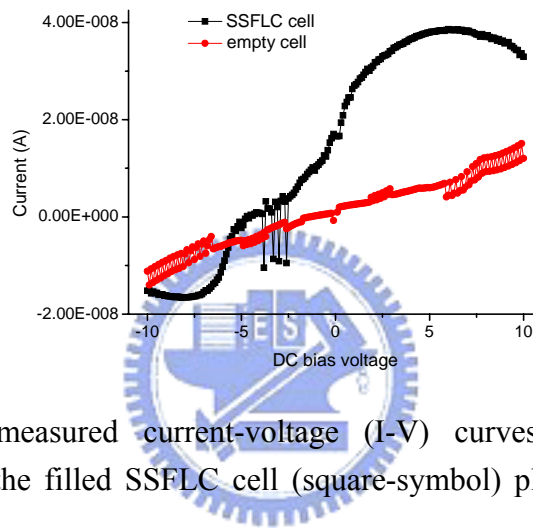


Figure 2-14 The measured current-voltage (I-V) curves of the empty cell (circle-symbol) and the filled SSFLC cell (square-symbol) plotted as a function of applied voltage.

The Preisach Model

The Preisach model of hysteresis [20] behavior in a ferroelectric film proposes that the ferroelectric film is formed has a bi-dimensional distribution of coercitive fields, called the Preisach distribution [21]. The major physical approach of the Preisach model was to find the meaning of the Preisach distribution for ferroelectric thin films. Two microscopic interpretations had been proposed: (1) it attributes the coercive field distribution to ferroelectric dipoles [22]; (2) it refers to the threshold voltage at which the independent domain switch [23]. The Preisach model can be applied to analyze the behavior of the ferroelectric liquid crystal [24]. In this study,

we use the Preisach model to describe the variation of the FLC capacitor as a frequency-dependent polarization reversal in SSFLC under an applied driving field. The spontaneous polarization of the FLC can directly couples with the external electric field. The polarization-electric field (P-E) curve of the FLC was shown in the Figure 2-15 [25].

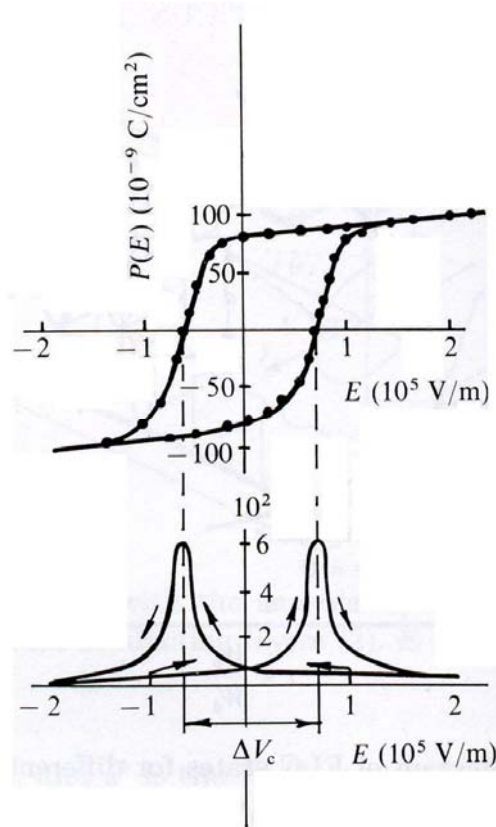


Figure 2-15 Hysteresis of macroscopic polarization $P(E)$ (top) and dielectric susceptibility $\chi(E) = \partial P / \partial E$ (bottom) for an FLC cell. Here ΔV_c is defined to be the width of hysteresis.

The FLC molecules can be aligned parallel or antiparallel to the applied electric field direction, and the transition from the antiparallel state to the parallel state is followed by the reversal of the polarization direction. The nonlinear capacitance of FLC cell can combine with a linear capacitance [26] to yield

$$C_{LC} = C_{lin} + \left(\frac{dp}{dV_{ext}} \right) \frac{S}{L} \quad , \quad (2-10)$$

where C_{lin} denotes the linear capacitance, V the applied voltage, S and L the area and the thickness of the capacitance, respectively. Here the nonlinear capacitance, which corresponds to the polarization reversal, can be deduced from the Preisach model. The individual dipoles in the FLC film add up to the total polarization and each of them had a rectangular hysteresis loop. The external applied field can interact with the dipoles to change their directions.

Assuming the direction of the dipoles in thermal equilibrium to exhibit a Gaussian distribution [27], the resulting total polarization P of the FLC film could be expressed as

$$P(V_{ext}) = FP \tanh \left[\delta (V_{ext} \mp V_C^\pm) \right]. \quad (2-11)$$

Here F is a factor reflecting the behavior of the loop is not saturated; δ is a constant with

$$\delta = V_C^{-1} \left[\log \left(\frac{1 + P_r / P_s}{1 - P_r / P_s} \right) \right], \quad (2-12)$$

P_s denotes the saturated polarization or the spontaneous polarization, and the V_c^\pm is the mean value of the individual coercive voltage. The (+) sign indicates an increase of V_{ext} , and the (-) sign a decrease of V_{ext} . The meaning of FP_s represents the proportion of the dipoles in the switching process of the non-saturated loop [29]. By combining Eq. (2-10) with Eq.(2-11), an expression of the FLC capacitance can be obtained

$$C_{LC} = C_{lin} + \frac{FP_s \delta}{\cosh^2 \left[\delta (V_{ext} \mp V_C^\pm) \right]} \frac{S}{L} \quad (2-13)$$

$$\text{and } \left. \frac{dP(-V)}{dV} \right|_v = \left. \frac{dP(+V)}{dV} \right|_{-v}.$$

Eq. (2-13) shows that the capacitance peaks in the C-V curve shall coincide with the polarization reversal point and the intensity of the peak relating to the amount of

switchable polarization [28].

2.5 Electrical Properties of SSFLC with and without nc-ZnO Doping

We shall focus in this section on the electrical properties of SSFLC test cells doped with nc-ZnO powder and the pure SSFLC. We shall apply the effective electronic circuit presented in section 2-4, to deduce the relation of the FLC capacitance with the applied voltage. All C-V curves were measured with the HP4284A LCR meter at room temperature. The cell gap and the area of our SSFLC test cells are $2\ \mu\text{m}$ and $180\ \text{mm}^2$, respectively. The FLC FELIX -017/100 mixture has a spontaneous polarization of $48.2\ \text{nC/cm}^2$ at room temperature.

The measured CV curves of pure FLC at four different frequencies of 100 Hz, 1K, 10K and 100KHz respectively are shown in the Figure 2-16(a), and the Figure 2-16(b) is an expanded view of the curves at the high frequencies of 10 K and 100 KHz. In general, the profiles of the C-V hysteretic loops vary with frequency. The peak values of the capacitances decrease with an increase of frequency and the voltage with maximum capacitance also changes. All the C-V curves are symmetric with respect to the 0V point.

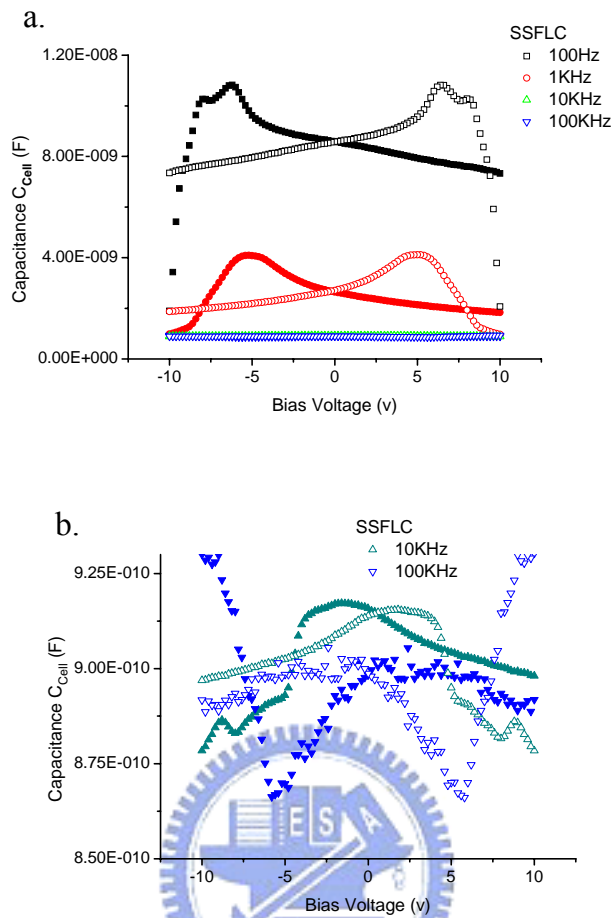


Figure 2-16 The capacitance (C_{LC}) versus the applied voltage on the pure SSFLC cell without doping at four different frequencies: (a) at 100Hz, 1KHz, 10KHz, and 100KHz; (b) An expanded view of the curves at the two highest frequencies 10KHz and 100KHz.

The Figure 2-17(a) shows the CV characteristic curves of the nc-ZnO doped SSFLC cell at four different frequencies of 100, 1K, 10K and 100KHz, respectively. These CV curves are similar to those of the pure FLC with some minor differences. Such as the C-V hysteresis loops exhibit a reversal behavior at 10K and 100KHz. In the following we shall apply the Preisach model to yield more detailed information about the doping effect of ZnO nanocrystals.

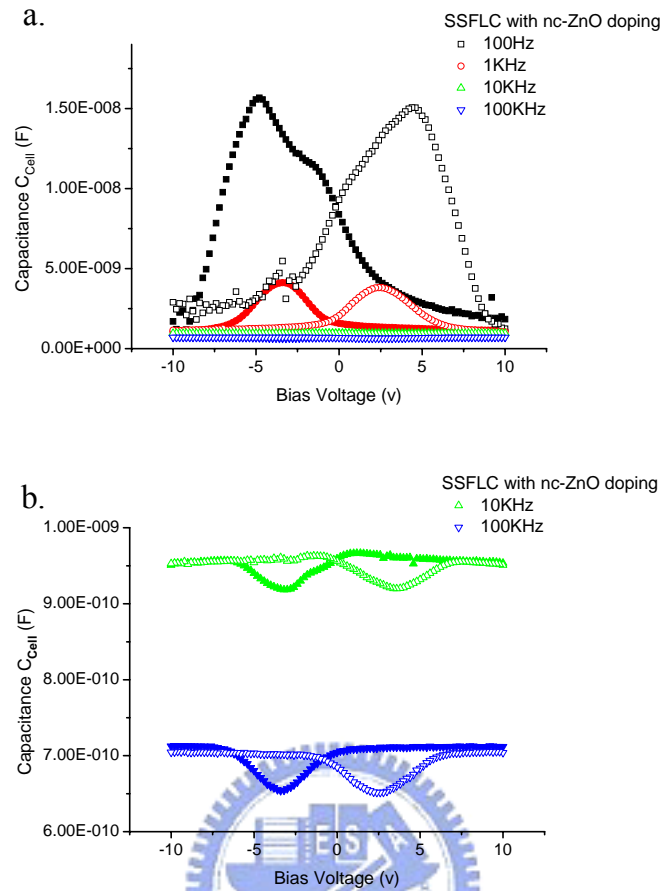


Figure 2-17 The capacitance (C_{LC}) versus the applied voltage on the nc-ZnO doped SSFLC cell at four different frequencies: (a) at 100Hz, 1KHz, 10KHz, and 100KHz; (b) An expanded view of the curves at the two highest frequencies 10KHz and 100KHz.

From the measured data, we found that the pure SSFLC can not be fitted with single Preisach model. It is considering that the FLC material FELIX 017-100 is a mixture and that it may possess several FLC dipole species with different responses at various field strength and frequencies. We therefore propose the Preisach model to have

$$C_{LC} = C_{lin} + (m_1 + m_2 + m_3 + m_4) \frac{S}{L} \quad (2-14)$$

with

$$m_1 = \frac{(FP_s)_1 \delta_1}{\cosh^2 [\delta_1 (V_{ext} \mp V_{C1}^\pm)]}, m_2 = \frac{(FP_s)_2 \delta_2}{\cosh^2 [\delta_2 (V_{ext} \mp V_{C2}^\pm)]},$$

$$m_3 = \frac{(FP_s)_3 \delta_3}{\cosh^2 [\delta_3 (V_{ext} \mp V_{C3}^\pm)]}, m_4 = \frac{(FP_s)_4 \delta_4}{\cosh^2 [\delta_4 (V_{ext} \mp V_{C4}^\pm)]}$$

Figure 2-18 presents the measured data (empty squares) and the fitting curve to Eq. (2-14) (black solid line) of the pure SSFLC at 100Hz. We need four linear Preisach terms to achieve a good fit to the data as indicated in Figure 2-19(a). The resulting fitting parameters δ , V_c^\pm , and FP_s , as described by Eq.(2-14) are summarized in Table 2-1.

The results of SSFLC with nc-ZnO doping are presented in Figure 2-18, with the measured data (empty triangle symbol), the fitting curve (black solid line) at 100Hz. Two linear Preisach terms are needed to yield a good fit of the data to Eq. (2-14) as shown in Figure 2-19(b). The resulting fitting parameters δ , V_c^\pm , and FP_s , as described by Eq. (2-14) are summarized in Table 2-2. At 100Hz, we found that the SSFLC with nc-ZnO doping has a higher capacitance peak and lower coercive voltage (the peak position) than the pure SSFLC.

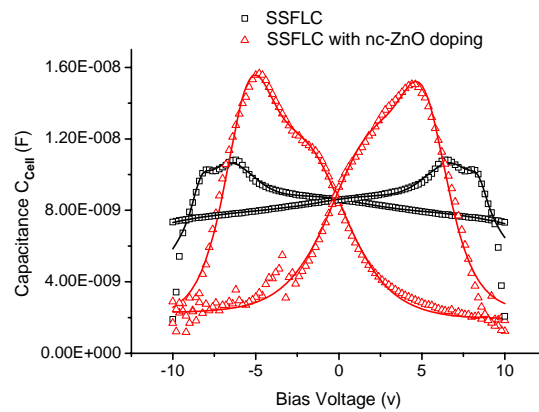


Figure 2-18 The experimental C-V curves (open symbols) and the fitting curves (solid lines) of the SSFLC test cells without and with nc-ZnO doping cells at 100Hz.

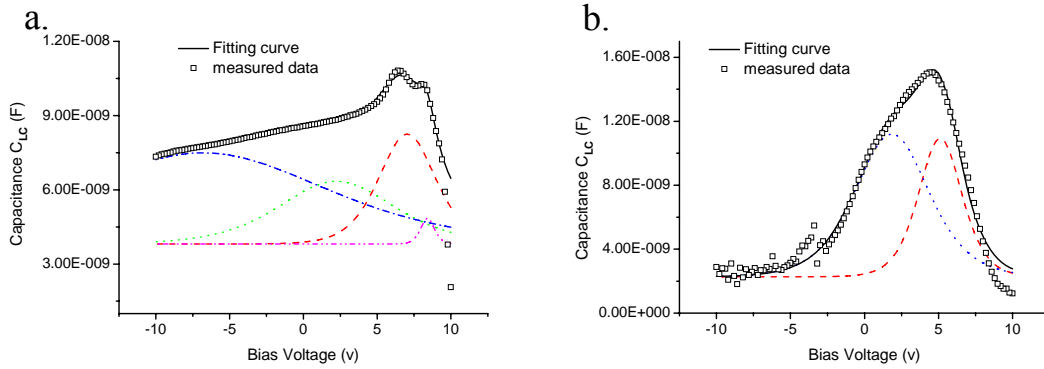


Figure 2-19 The fitting results of the measured data of (a) the SSFLC cell, and (b) the SSFLC cell with nc-ZnO doping at 100Hz. The solid lines are the fitting curve and the symbols are the measured data. (a) The four curves with dash, dot, dash-dot and dash-dot-dot, respectively, represent the corresponding Preisach terms involved. (b) The dash and dot lines represent the corresponding Preisach terms involved in the nc-ZnO doped SSFLC cell.

In Figure 2-19, the experimental data can be synthesized with several Preisach terms because the molecules of FLC FELIX 017-100 may possess several FLC dipole species. Because the polarization of the FLC couples directly to the external electric field, these molecular dipole species may exhibit different responses at various field strength and frequencies. At the frequency 100Hz, the ZnO nano dots can effectively “glue” their surrounding FLC dipoles together and yield an improved alignment as shown in the imaging polarimetric investigation. This novel effect is possible in view that these nc-ZnO possess fairly large dipole moments and could affect the FLC molecules via dipolar interaction, which simplifies the Preisach terms needed at 100 Hz from four to two with nc-ZnO doping. It is also interesting to point out that the peak positions (*i.e.*, the coercive voltage) of the Preisach terms with the dashed and the dotted curves are similar for the two cells but the SSFLC cell with nc-ZnO doping yields a higher peak height. The SSFLC cell with nc-ZnO doping does not exhibit another two Preisach terms (the dash-dott and dash-dot-dot lines), which are present in the pure SSFLC. This appears to affirm that ZnO nanocrystals could effectively

connect the FLC dipole species and simplify the field-induced responses.

Table 2-1 The fitting parameters of the pure SSFLC cell to Eq. (2-14) at different frequencies.

	100Hz	1KHz	10KHz	100KHz
δ_1	0.36642			-0.36642
V_{c1}^{\pm} (V)	± 7.0354	± 5.38644	± 3.64075	± 5.590
$(FP_s)_1$ (C/mt ²)	1.277×10^{-10}	7.297×10^{-11}	3.458×10^{-13}	1.480×10^{-12}
δ_2	0.191199			-0.191199
V_{c2}^{\pm} (V)	± 2.24519	± 1.7003	± 0.355235	± 1.98496
$(FP_s)_2$ (C/mt ²)	1.473×10^{-10}	8.547×10^{-11}	1.617×10^{-12}	1.614×10^{-12}
δ_3	0.885003			-0.885003
V_{c3}^{\pm} (V)	∓ 6.82148	∓ 7.38824	∓ 10.7792	∓ 11.2531
$(FP_s)_3$ (C/mt ²)	5.589×10^{-10}	2.322×10^{-10}	2.866×10^{-12}	7.564×10^{-12}
δ_4	1.6201			
V_{c4}^{\pm} (V)	± 8.4126			
$(FP_s)_4$ (C/mt ²)	7.257×10^{-12}			

From the Table 2-1, the pure SSFLC cell requires four linear Preisach terms model was used to fit its measured at 100Hz, but only three are needed for 1KHz and 100KHz. Both the switchable polarization (FP_s) and the coercive voltage (V_c^{\pm}) decrease with an increase of frequency. The parameters δ_1 , δ_2 , δ_3 , and δ_4 are positive at frequencies below 100KHz. At 100KHz, the C-V curve exhibits a reversal phenomenon. The parameter δ_1 , δ_2 and δ_3 became negative with magnitudes similar to their positive values.

Table 2-2 presents the fitting parameters of the SSFLC cell with nc-ZnO doping cell. Only two linear Preisach terms are needed at 100Hz, and it is reduced to one at 1K, 10K, and 100KHz. The δ_1 and δ_2 of the SSFLC with nc-ZnO doping cell are different from the corresponding values in the pure SSFLC cell. The reversal of C-V curve occurs at 10KHz and the δ parameters change sign from positive to negative. It is to know that the FLC molecules naturally try to align with the largest permittivity component along the external field. If the frequency of the electric field is so high that it cannot couple with the spontaneous polarization. Therefore, the FLC molecules will remain in (or return to) the almost fully switched state and do not contribute to the nonlinear part of the capacitance. For the reason, the inversion of the C-V curve is associated to the inversion of the dielectric $\delta\epsilon$. When the spontaneous polarization is proportion to the dielectric biaxiality, the C-V hysteresis loop will show an inversion at higher frequencies [30]. The switchable polarization (FP_s) decreases with an increase of frequency from 100 Hz to 1 KHz, but becomes increase with frequency from 10KHz to 100KHz. But the coercive voltage always decreases with an increase of frequency. At higher frequency the applied field changes direction before the FLC molecules reach their final position for the applied field magnitude, so that the contribution of the molecules to the dielectric constant decrease [30]. Hence, the switchable polarization (FP_s) decreases with an increase of frequency. However, after the C-V hysteresis loop shows an inversion, the behavior of the switchable polarization (FP_s) may also inverse.

Table 2-2 The fitting parameters of the SSFLC cell with nc-ZnO doping to Eq. (2-14) at different frequencies

	100Hz	1KHz	10KHz	100KHz
δ_1	0.509512		-0.509512	
V_{c1}^{\pm} (V)	± 5.11285	± 2.5093	± 3.55682	± 2.50275
$(FP_s)_1$ (C/mt ²)	1.889×10^{-10}	6.083×10^{-11}	8.376×10^{-13}	1.245×10^{-12}
δ_2	0.29875			
V_{c2}^{\pm} (V)	± 1.84602			
$(FP_s)_2$ (C/mt ²)	3.319×10^{-10}			

Figure 2-20 shows the measured data of the pure SSFLC (open squares) and the SSFLC with nc-ZnO doping (open triangles) at 1KHz and their corresponding fitting curves (solid lines) to Eq. (2-14). Figure 2-21 displays the linear Preisach terms involved in the pure SSFLC and SSFLC doped nc-ZnO at 1KHz. Clearly, the pure SSFLC cell requires three Preisach terms to successfully synthesize the experimental curve, but for the SSFLC with nc-ZnO doping only one is needed at the same frequency 1KHz. The coercive voltage of the SSFLC with nc-ZnO doping is about the averaged value of the two coercive voltages of the Preisach terms (the dash and dot lines) used in the pure SSFLC. This again affirms that ZnO nanocrystals could effectively connect the FLC dipole species and simplify the field-induced responses.

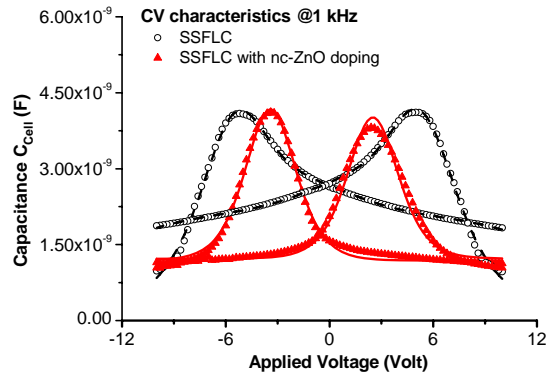


Figure 2-20 The experimental C-V curves (empty symbols) and their fitting results (solid lines) of the SSFLC cells without and with nc-ZnO doping at 1 kHz.

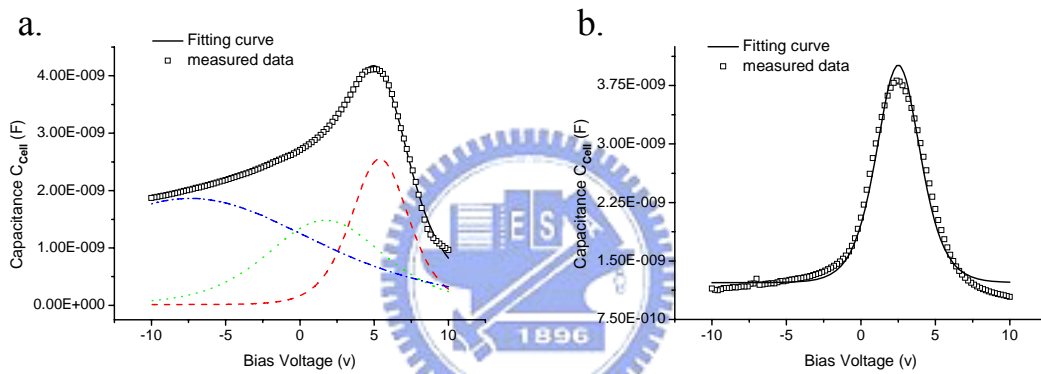


Figure 2-21 The fitting curves to Eq. (2-14) of (a) the SSFLC cell and (b) the SSFLC cell with nc-ZnO doping at 1 kHz. The symbols are the measured data. In (a) the three curves with dash, dot, and dash-dot, respectively, represent the Preisach terms involved and the solid line is the summation of all the three terms. (b) The solid line is the fit to the single-component Preisach model.

Figures 2-22 and 2-23 present the measured data of the pure SSFLC (open squares) and the SSFLC cell with nc-ZnO doping (open triangles) and the corresponding fitting curves (solid lines) at 10KHz and 100KHz, respectively. At 10 kHz, the SSFLC cell doped with nc-ZnO cell exhibits a reversal C-V hysteretic curve, however the pure SSFLC cell displays similar CV reveal behavior at 100 kHz. The experimental data of the pure SSFLC cell require a good fit to Eq. (2-14) with three linear Preisach terms at 10K, and at 100 kHz but the SSFLC cell doped with nc-ZnO

only one term is sufficient. The capacitance of the SSFLC cell with nz-ZnO doping is larger than the pure SSFLC cell at 10KHz, but at 100KHz the situation is reversed. According to the above mentioned reason about the inversion of C-V curve, when the FLC molecules cannot couple with the spontaneous polarization, the FLC molecules will remain in (or return to) the almost fully switched state and do not contribute to the nonlinear part of the capacitance [30]. It is considered that after FLC molecules doped with nc-ZnO, the spontaneous polarization of FLC doped with nc-ZnO may produce some change which is not equal to the pure FLC. Even at the same frequency of 10KHz, the spontaneous polarization of FLC with nc-ZnO doping cannot couple the electric field. Comparing the Figure 2-16(b) and 2-17(b), the linear capacitance of the SSFLC seems almost the same value but the linear capacitance of the SSFLC with nc-ZnO doping shift to lower value with the increase of frequencies. In a word, with the increase of frequencies, the decreasing rate of SSFLC doped with nc-ZnO is faster than that of SSFLC. It might be the nc-ZnO make the FLC molecules become more sensitive to the external frequencies. Therefore, the capacitance of the SSFLC cell with nz-ZnO doping is larger than the pure SSFLC cell at 10KHz, but at 100KHz the situation is reversed.

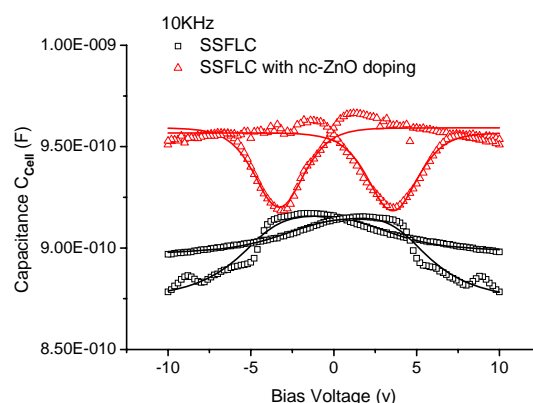


Figure 2-22 The experimental C-V curves (open symbols) and the fitting curves (solid lines) of the SSFLC cells without (square) and with (triangle) nc-ZnO doping at 10 kHz.

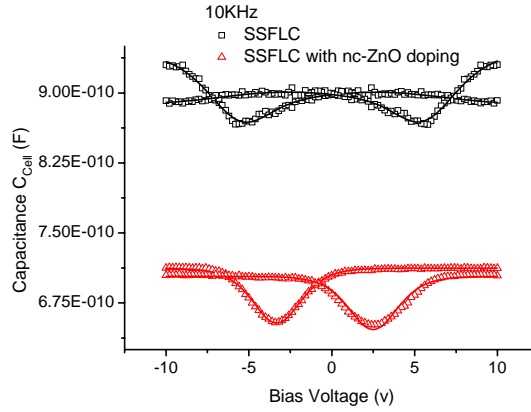


Figure 2-23 The experimental C-V curves (open symbols) and the fitting curves (solid lines) of the SSFLC cells without (square) and with (triangle) nc-ZnO doping at 100 kHz.

In summary, both the SSFLC cells with and without nc-ZnO doping exhibit symmetric CV hysteretic curves with respect to 0V. By fitting the measured data to the Preisach model, different numbers of linear Preisach terms are required at different frequencies, indicating that the SSFLC used possesses several FLC dipolar species with different responses to the applied voltage and frequencies. At higher frequencies the external driving field changes its direction before the FLC molecules can settle down to their final orientations [29]. Therefore, both the maximum capacitances and the amount of the switchable polarization (FP_s) decrease with an accompany of decreasing coercive voltage (V_c^\pm) as the applied frequency is increased. The maximum capacitance in the C-V curves for the ferroelectric material reflects beginning of polarization reversal rather than maximum molecular density near the coercive voltage [31]. The dipoles of the ZnO nanocrystal can effectively tie up the surrounding FLC species to perform a collective switching under an external driving field. The FLC doped with ZnO nanocrystals exhibits a lower coercive voltage. The difference between the maximum and minimum of the C-V curves of the SSFLC cell doped with nc-ZnO is larger than that of the pure SSFLC cell. Based on these results,

doping with ZnO nanocrystals appears to be a simple while effective approach to improve the application properties of existing FLC materials.



Chapter 3

Electro-Optical Switching Dynamics of SSFLC Cells with and without nc-ZnO Doping

3.1 Model of Electro-Optical Response of a SSFLC Cell

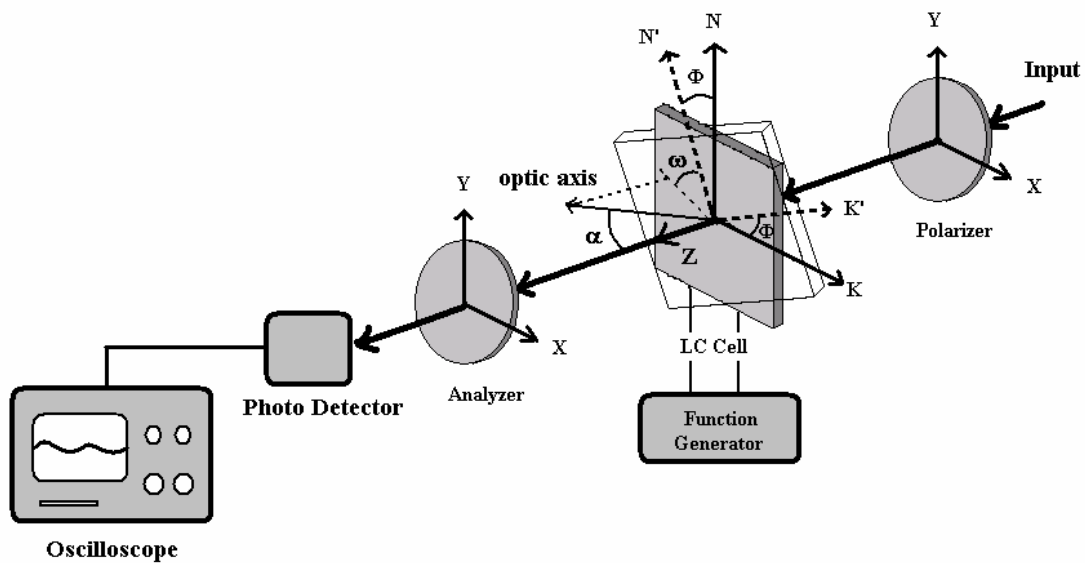


Figure 3-1 Schematic diagram showing the time-resolved electro-optical characterizing apparatus used in this study.

Figure 3-1 presents the schematic diagram of the time-resolved electro-optical characterizing apparatus used in this study. This system includes a light source, a polarizer, a rotation stage for sample cell, an analyzer, a function generator, a photo detector, and an oscilloscope. A laser diode with a wavelength 670 nm was used as the light source and the propagation direction was set to along the z-axis. A SSFLC test cell was mounted on the rotation stage to be rotated about the z-axis. The fast axis of the polarizer is along to the x-axis. The function generator applies a waveform of square-wave on the SSFLC cell. The light beam transmitting through the SSFLC cell

was analyzed with the analyzer, which was set to cross with the polarizer, and then was detected with a photo detector. An oscilloscope was used to record the waveforms of signal from photo detector and the driving field from the function generator. The rubbing direction \mathbf{K} of SSFLC cell was initially along the X-axis of the laboratory coordinate system. The sample cell can be rotated about the Z-axis with an angle of Φ . The optic axis of the FLC film projects onto the substrate surface (\mathbf{K} - \mathbf{N} plane) to yield an azimuthal angle of ω relative to the rubbing direction \mathbf{K} .

By applying Jones' calculus, an expression of the optical field incident on a photo-detector can be derived

$$\begin{bmatrix} E'_x \\ E'_y \end{bmatrix} = E_o \begin{bmatrix} 1 & 0 \\ 0 & 0 \end{bmatrix} \begin{bmatrix} \cos(\Phi + \omega) & \sin(\Phi + \omega) \\ -\sin(\Phi + \omega) & \cos(\Phi + \omega) \end{bmatrix} \begin{bmatrix} -i \sin(\frac{\Gamma}{2}) & \cos(\frac{\Gamma}{2}) \\ -\cos(\frac{\Gamma}{2}) & i \sin(\frac{\Gamma}{2}) \end{bmatrix} \begin{bmatrix} \cos(\Phi + \omega) & -\sin(\Phi + \omega) \\ \sin(\Phi + \omega) & \cos(\Phi + \omega) \end{bmatrix} \cdot \frac{1}{\sqrt{2}} \begin{bmatrix} 0 \\ 1 \end{bmatrix} \quad (3.1)$$

The SSFLC cell is oriented with its optic axis pointing to a direction with a polar angle of α relative to the beam propagation direction (Z-axis). The geometry is depicted in the molecular frame shown in Figure 3-2.

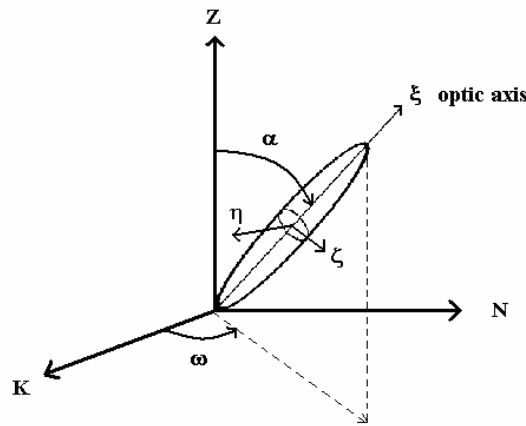


Figure 3-2 Schematic diagram showing the orientational relationship between the molecular frame (ξ, η, ζ) and the sample frame ($\mathbf{K}, \mathbf{N}, \mathbf{Z}$)

The SSFLC cell behaves like a wave-retarder with an optical retardance $\Gamma(\alpha)$ given by [15].

$$\Gamma(\alpha) = \frac{2\pi}{\lambda} d \left(\frac{1}{\sqrt{\frac{1}{n_e^2} \sin^2 \alpha + \frac{1}{n_o^2} \cos^2 \alpha}} - n_o \right) \quad (3.2)$$

where d is the thickness of the SSFLC cell, and λ is the wavelength of light source used. By using Eq. (3.1), the irradiance on the detector can be expressed as

$$I_T = E'_x E'^*_x + E'_y E'^*_y = \frac{I_0}{2} \sin^2 \left(\frac{\Gamma}{2} \right) \cos^2 [2(\Phi + \omega)] \quad (3.3)$$

Assuming the angle Φ of the SSFLC cell to be changed from 0° to 360° , the time-resolved optical transmission signal can be sampled and recorded with the oscilloscope at each Φ . Eq. (3-3) suggests that the resulting time-resolved angular pattern of the optical irradiance on the detector can be expressed as

$$\bar{I}(\Phi) = b(t) + c(t) \cos^2 [2(\Phi + \omega(t))], \quad (3.4)$$

where $b(t)$ denotes an isotropic part of the dynamic alignment of SSFLC, $c(t) = 0.5 I_0 \sin^2(\Gamma/2)$ represents the angularly aligned component of the SSFLC film, and $\omega(t)$ is the azimuthal angle of the optic axis projected onto the cell substrate. We recorded a total of 37 angular patterns from $\Phi = 0^\circ$ to 360° at each specific time instant. The measured patterns (see the black squares in Figure 3-3) can be fitted to Eq. (3-4) (the solid line) to deduce the parameters $a(t)$, $b(t)$, and $\Phi(t)$. Notice that upon the reversal of the sign of an applied field, all the molecules in the ferroelectric phase switch by rotation about a tilt cone. Due to the conic motion, $c(t)$ varies with polar angle α . The detailed information about the conic motion of SSFLC can be deduced by analyzing the dynamic EO response patterns.

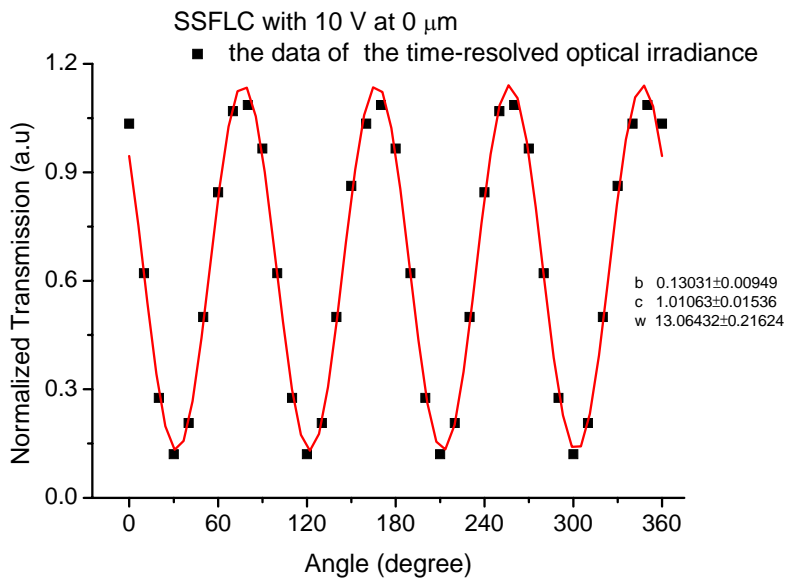
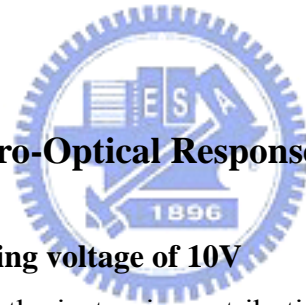


Figure 3-3 Time-resolved angular pattern (symbols) of optical transmission through a SSFLC cell with 10 V at 0 μ sec and the corresponding fitting curve (solid line) to Eq. (3-4).



3.2 Time-Resolved Electro-Optical Response of SSFLC Cell

3.2.1 SSFLC cell with a driving voltage of 10V

According to section 3.1, the isotropic contribution, angular alignment term, and the projected angle of the optic axis of a SSFLC cell can be deduced from the fitting procedure. In Figure 3-4, we present the time-resolved electro-optical azimuthal patterns of an undoped SSFLC cell. The transmission intensity at each time instant had been normalized to the maximum transmission of the SSFLC cell at zero driving field, which is indicated by the solid curve in Figure 3-4. The other lines with symbols represent the azimuthal patterns recorded at five different delay times of the SSFLC cell driven with an amplitude +10V (Figure 3-4(a)) and -10V (Figure 3-4(b)) of square wave form. The high dichotic ratio of the patterns indicated the SSFLC cells used in this study to have high alignment quality. It is interesting to notice that at the very beginning of the field-on period at 0 μ sec the transmission intensity is larger than

that without driving field and the direction of the FLC molecule is rotated about 30 degrees. The symmetry axis of the azimuthal patterns rotates rapidly with an accompany of a reduction of modulation depth. When the electric field is applied for an extended period, the amplitude of the azimuthal pattern becomes larger than the initial value while the orientation of the azimuthal pattern does not change significantly. Similar behavior occurs in the negative field-on period shown in Figure 3-4(b).

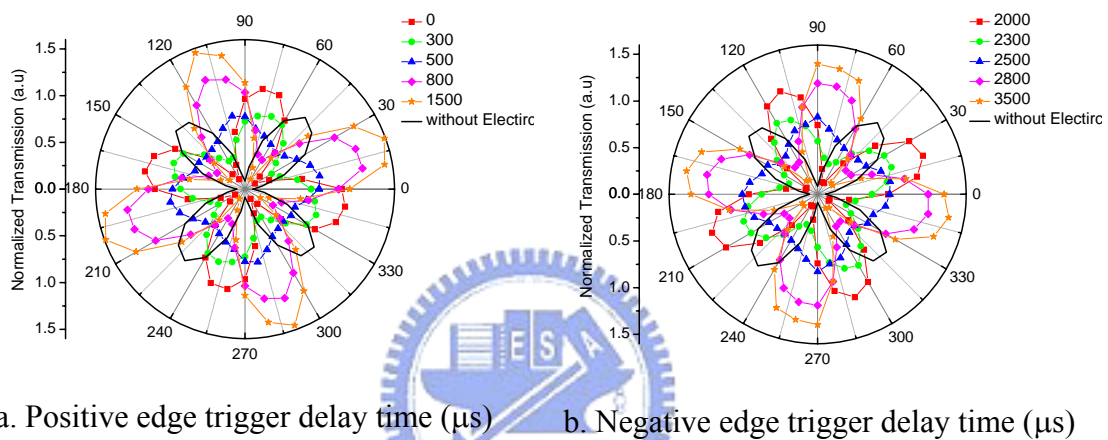


Figure 3-4 The transient electro-optical azimuthal patterns of a SSFLC cell recorded at five different delay times. The driving field is (a) +10V, (b) -10V square waveform with a field-on duration of 800 μs .

These time-resolved azimuthal patterns can be fitted to Eq. (3-4) to deduce the parameters $b(t)$, $c(t)$, and $\omega(t)$, which are presented in Figure 3-5. The switching time course of the SSFLC director shown in Figure 3-5(b) appeared to be symmetric in both the positively and negatively driven cycles. The contrast ratio of the optical transmission decreased during the field-on period, as shown by a rapid increase of the isotropic component $b(t)$. The isotropic component then slowly decreased with an accompanying increase of $c(t)$. The angularly aligned component $c(t)$ can be increased dynamically to about 1.4 times of its zero-field case.

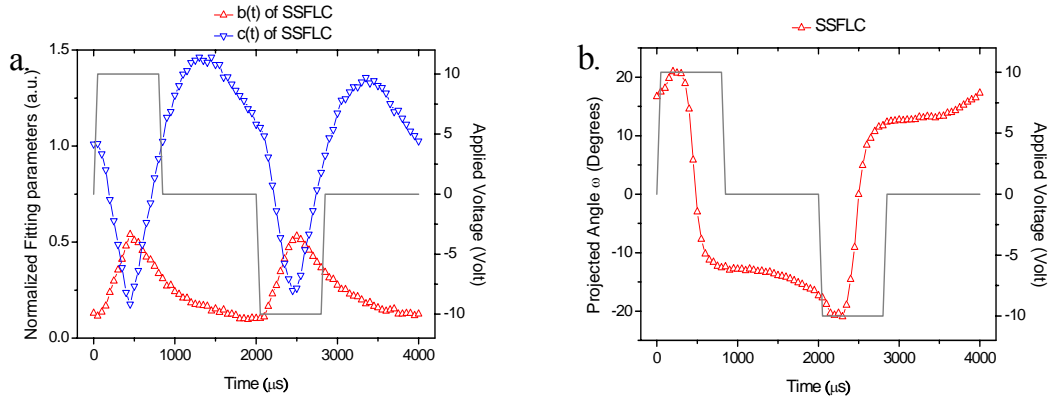


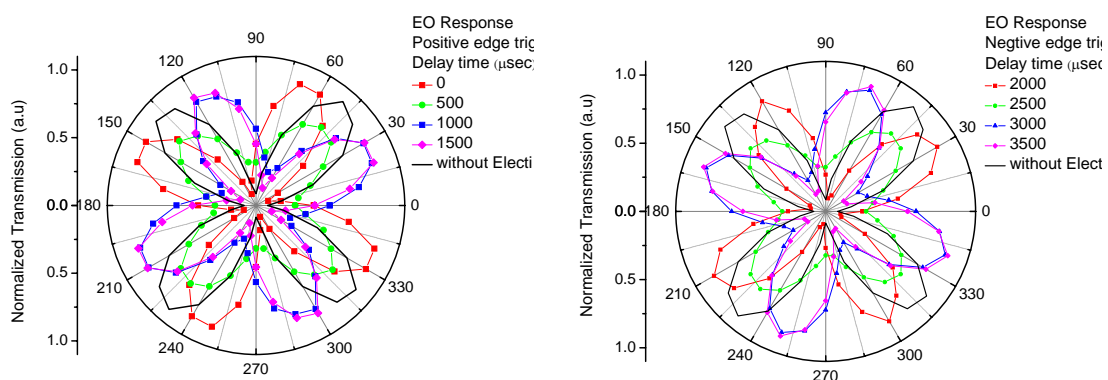
Figure 3-5 (a) Fitting parameters (symbols) of the time-resolved EO azimuthal patterns and the applied voltage (solid line) are plotted as a function of time. (b) The deduced orientation angle of the optic axis of FLC film is shown. The rubbing direction of the FLC cell with is along the 0 degree.

As shown in Figure 3-5(b), the projected angle was found to increase first and then reverses rapidly to the other direction. Similar behavior occurs in the negative driving cycle. The C-V curve at 100 Hz shown in Figure 2-16 indicates that the capacitance of the FLC film first increases gradually from 0V to +5V (or -5V). The FLC capacitance rapidly increases to a peak at a voltage about 6V and then decreases when the applied voltage increases further. Therefore when the applied voltage is switched on from 0 to 10V, the FLC molecules will experience a field strength depending on the dynamic film capacitance. When the transient applied field strength on the film crosses 6V, a reversal behavior will be observed. The response time of $\omega(t)$ can be estimated to be $\tau_{10-90}=200 \mu\text{sec}$. Notice that the electro-optical response time can be calculated with $\tau = \gamma/P_s E_{\perp}$. Here γ denotes the rotational viscosity, P the spontaneous polarization of FLC and E_{\perp} the applied electric field. By using the available material parameters of Felix 017/100: $\gamma = 4.8 \times 10^{-5} \text{ N} \cdot \text{sec}/\text{cm}^2$, $P_s = 46.74 \text{ nC}/\text{cm}^2$, and the applied field strength $E_{\perp} = 5 \times 10^6 \text{ V}/\text{cm}$, we obtain $\tau = 207 \mu\text{sec}$, which agrees well with the measured

electro-optical response time of the SSFLC.

3.2.2 SSFLC cell with a driving voltage of 5V

Figure 3-6 displays the time-resolved electro-optical azimuthal patterns of a undoped SSFLC cell at a driving voltage of $\pm 5V$. Similar to the case shown in Figure 3-5 with $\pm 10V$, all the transmission intensity patterns are normalized to the maximum transmission of the SSFLC cell at zero applied field. The solid line indicates the EO transmission curve without an electric field and the curves with symbols are the measured patterns at four different delay times with a driving amplitude of $+5V$ (Figure 3-6(a)) and $-5V$ (Figure 3-6(b)). We can see that the transmission intensity at $0 \mu s$ is similar to that with no field applied and the direction of the FLC molecule rotated about 15 degrees only (30 degrees in the case of 10V). The symmetry axis of the azimuthal patterns rotated rapidly with a decrease of modulation depth. When the external electric field is applied for a periodic time of $1500 \mu s$, the normal transient amplitude of the azimuthal pattern in 5V does not increase beyond 1, but it in 10V is about 1.5 (see Figure 3-4).



a. Positive edge trigger delay time (μs) b. Negative edge trigger delay time (μs)

Figure 3-6 The normalized transient electro-optical azimuthal patterns of a SSFLC cell at four different delay times. The driving field amplitude is (a) $+5V$, and (b) $-5V$. The rubbing direction of the FLC cell is set to at 0 degree.

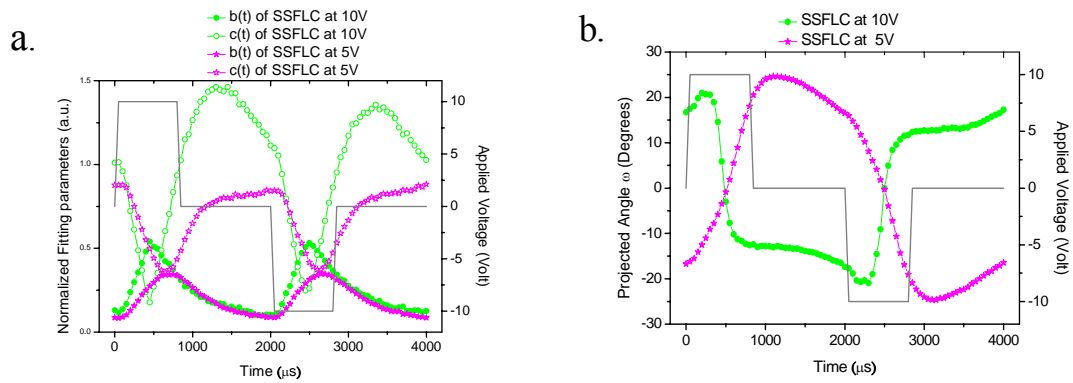


Figure 3-7 Comparison of the fitting parameters at two different applied voltages. The curves with circles represent the data with ± 10 V and the curves with star symbol are the data measured with ± 5 V. (a) Fitting parameters (symbols) of the time-resolved EO azimuthal patterns and the applied voltage (solid line) are plotted as a function of time. (b) The deduced orientation angle of the symmetry axis of FLC film is shown.

By fitting the experimental patterns to Eq. (3-4), we can determine $b(t)$, $c(t)$, and $\omega(t)$ as function of time. The comparison of the fitting results with driving voltages of ± 5 V and ± 10 V are presented in Figure 3-7. The larger external driving field can reorient FLC molecules with a faster speed. However, the maximum value of the isotropic term with ± 5 V is smaller than that with ± 10 V, whereas the minimum value of the uniaxial term becomes larger than that with ± 10 V. This was because that the higher driving field, the more reorientation angle of the FLC molecules would experience. In the Figure 3-7(b), at the turn-on instant with 5V, the symmetry axis of the azimuthal pattern switches monotonically to the other direction, which is unlike to the case with 10V. This is because that by comparing to the C-V curve shown in Figure 2-16 at 100Hz, the voltage with the maximum capacitance occurs at a value larger than ± 5 V. Therefore the FLC molecules will rotate reversely with an applied voltage ± 10 V. But the molecules will rotate continuously along one direction when the applied voltage is ± 5 V.

At a driving voltage of $\pm 5\text{V}$, the time courses yields a rising time of the electro-optical response to be $\tau_{10-90}=650\ \mu\text{sec}$, which is about 3.3 times longer than that with $\pm 10\text{V}$. Therefore, the response time of the FLC molecules in a SSFLC cell is sensitively related to the dynamic capacitance of the cell which determines how high the applied voltage will be felt by the FLC molecules. The total rotated angle of the symmetry axis of the cell with $\pm 5\text{V}$ is larger than that with $\pm 10\text{V}$ by 7.6° , which is also caused by different electrical response of the SSFLC cell at different applied voltages.

3.3 Time-Resolved Electro-Optical Response of SSFLC Cell with nc-ZnO Doping

3.3.1 nc-ZnO doped SSFLC cell with a driving voltage of 10V

In this section, the time-resolved EO response of a SSFLC cell doped with the ZnO nanocrystal powder will be reported. The transient electro-optical azimuthal patterns of a pure SSFLC cell and a SSFLC cell doped with nc-ZnO powder are presented in the Figure 3-8. To perform a proper comparison, all the azimuthal patterns are normalized to the highest transmission intensity of the pure SSFLC cell. Although the dark state of the nc-ZnO-doped SSFLC cell is about the same as that of the pure SSFLC cell, the maximum optical transmission of the nc-ZnO-doped SSFLC cell is about 2.3 times larger than that of the pure SSFLC cell. Hence, doping with ZnO nanocrystals appears to be effective to improve the optical transmission property of a SSFLC cell.

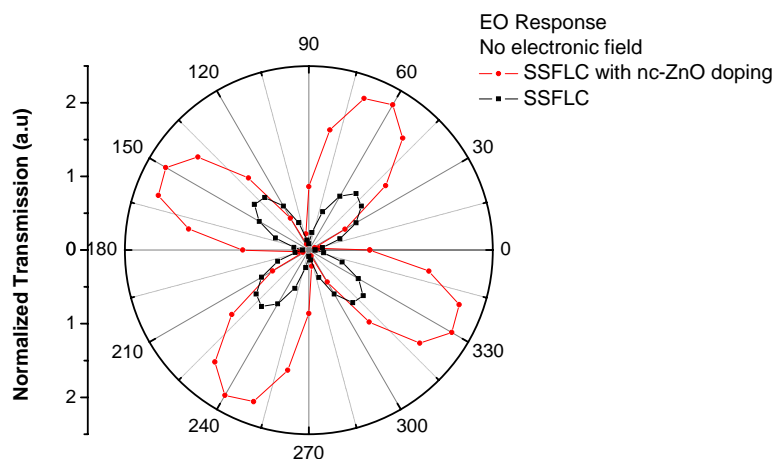
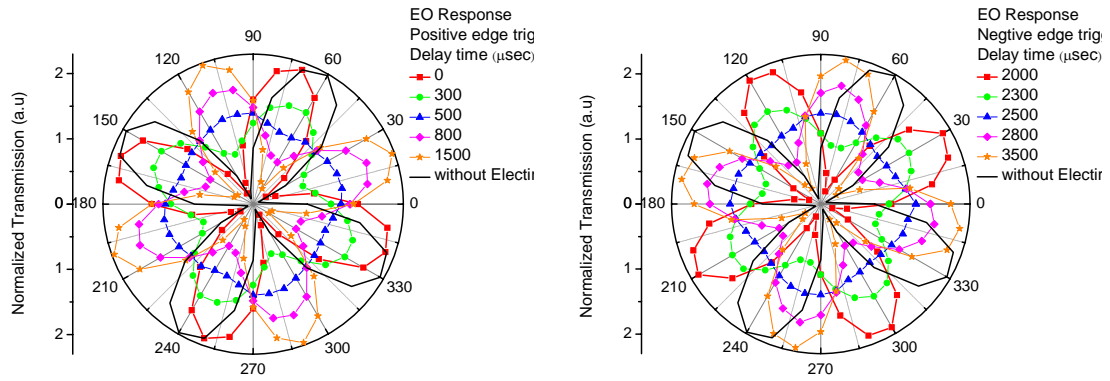


Figure 3-8 The normalized transient electro-optical azimuthal patterns of the pure SSFLC (square symbol) and the SSFLC with nc-ZnO doping (circle symbol) cells aligned with RN1182 were presented at no driving field amplitude.

If the orientations of FLC molecules are aligned along the rubbing direction, the direction with the maximum transmission will occur at 45° relative to the crossed polarizer-analyzer. From Figure 3-8, we found that the molecular orientations in the pure SSFLC cell and in the nc-ZnO-doped SSFLC cell are about 5° and 15° off from the rubbing direction. The result agrees with what was observed with imaging polarimetry shown in the Figure 2-7.

Figure 3-9 presents the time-resolved electro-optical azimuthal patterns of the SSFLC cell with nc-ZnO. The solid line indicates the EO pattern of the nc-ZnO doped cell without an applied field and the other curves with symbols are the patterns at five different delay times driven with a waveform of +10 V square pulse (Figure 3-9(a)) and -10V square pulse (Figure 3-9(b)), respectively. The high dichotic ratio of the patterns indicates the SSFLC cell doped with nc-ZnO to have a high alignment quality. Similar to what had been observed on the pure SSFLC cell, at the beginning of the driving cycle, the transmission intensity at $0 \mu\text{s}$ is rotated about $+10^\circ$ at positive driving cycle and about -30° at negative driving cycle. The symmetry axis of the

azimuthal patterns rotates rapidly with a reduction of modulation depth. The similar behavior occurs in the negative driving cycle.



a. Positive edge trigger delay time (μs) b. Negative edge trigger delay time (μs)
Figure 3-9 The normalized transient electro-optical azimuthal patterns of a SSFLC cell doped with nc-ZnO were presented at five different delay times. The driving field amplitude is (a) +10V, and (b) -10V.

By fitting the measured patterns to Eq. (3-4), the time courses of $b(t)$, $c(t)$, and $\omega(t)$ of the nc-ZnO doped SSFLC cell driven with ± 10 V can be retrieved. The results are presented in Figure 3-10. The switching process of $\omega(t)$ shown in Figure 3-10(b) is symmetric with the positive and negative driving pulses. *The switching speed of the nc-ZnO doped SSFLC cell ($\tau_{10-90}=100\mu\text{s}$) is faster than that of the pure SSFLC cell ($\tau_{10-90}=200\mu\text{s}$).* The total switching angle of the nc-ZnO doped SSFLC cell with ± 10 V driving pulse is equal to the cone angle of 55.1° .

The dichroic ratio $c(t)/b(t)$ of the optical transmission patterns decreases rapidly at the beginning of the field-on cycle. After the isotropic component $b(t)$ reaches a maximum, it then decreases slowly with an accompanying increase of $c(t)$. Although the time courses of the isotropic terms for the pure and the nc-ZnO doped SSFLC cells are similar, the alignment term $c(t)$ of the nc-ZnO doped SSFLC cell can reach a much higher value than that of the pure SSFLC cell during the field-free period, indicating that *the dynamic alignment is much improved in the nc-ZnO doped*

SSFLC cell.

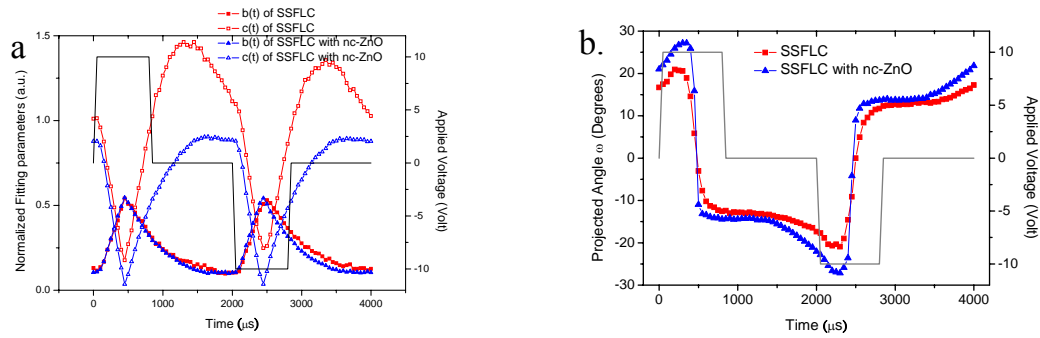


Figure 3-10 Comparing the parameters with two different cells at ± 10 V, the square symbol was SSFLC and the triangle symbol was SSFLC with nc-ZnO doping. (a) Normalized fitting parameters (symbols) of the EO azimuthal patterns and the applied voltage (solid line) were plotted as a function of time. (b) The deduced orientation angle of the optic axis of FLC film was shown. The rubbing direction of the FLC cell with was along the 0° .

3.3.2 nc-ZnO doped SSFLC cell with a driving voltage of 5V

The same measurements were repeated with a driving voltage ± 5 V. The results are shown in Figure 3-11. The solid line indicates the EO azimuthal pattern without an applied field and other curves with symbols are the azimuthal patterns taken at five different delay times with a driving waveform of +5V square pulse (Figure 3-11(a)) and -5V square pulse (Figure 3-11(b)), respectively. The amplitudes and the directions of the transient azimuthal patterns change with delay time and field polarity. At the beginning of the driving cycle, the maximum transmission at $0 \mu\text{s}$ occurs at a direction similar to that without an applied field, indicating that the FLC molecules do not rotate at the rising edge of the +5V driving pulse. On contrast, the FLC molecules can rotate about -30° at the driving edge of the -5V pulse (see Fig. 3-11(b)). This asymmetric behavior is caused by that nc-ZnO doping causes the FLC molecules to lie closer to the substrate plane when the positive field is just turned on. Therefore the initial field-induced ferroelectric torque is too weak to cause a rotation of the LC

director. After some delay time, the angle between the spontaneous polarization and the applied field increases, and the symmetry axis of the azimuthal patterns rotates with an increasing speed.

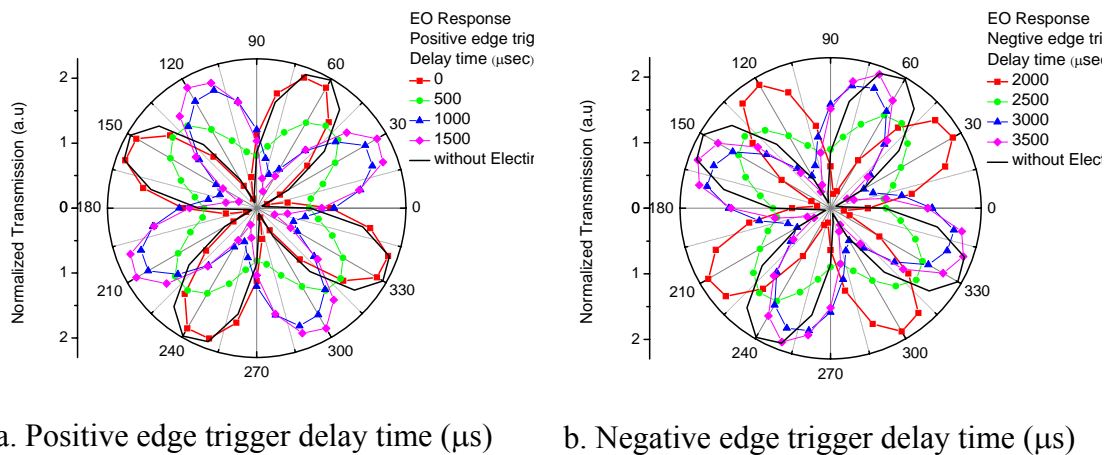


Figure 3-11 The normalized transient electro-optical azimuthal patterns of a SSFLC with nc-ZnO doping cell are presented at four different delay times. The driving field amplitude is (a) +5V, and (b) -5V.

The time courses of $b(t)$, $c(t)$, and $\omega(t)$ of the nc-ZnO doped SSFLC cell with driving voltages of $\pm 5V$ and $\pm 10V$ are presented in Figure 3-12. The switching curves $\omega(t)$ of the SSFLC director shown in Figure 3-12(b) indicate that the rotation speed is related to the applied field. As shown in Figure 2-16, the capacitance of the FLC film first increases gradually from 0V to +5V (or -5V). After that, the FLC capacitance rapidly increases to a peak at a voltage about 6V and then decreases when the applied voltage is increased further. Therefore when the applied voltage is switched on from 0 to 10V, the FLC molecules will experience an applied field strength depending on the dynamic film capacitance. When the transient voltage on the film crosses 6V, a reversal phenomenon will be observed. However, no such reversal shall be observed if the applied voltage is lower than 5V. The switching time of the electro-optical response with the driving voltage of $\pm 5V$ is $\tau_{10-90}=600 \mu\text{sec}$, which is about 6 times slower than that with $\pm 10V$. The dichroic ratio of the optical

azimuthal patterns first decreases during the field-on period. Due to a faster initial rotation speed with the $\pm 10\text{V}$ driving pulse, $c(t)$ can be reduced to a smaller value and $b(t)$ be increased to a higher value than that with $\pm 5\text{V}$. However, the alignment term $c(t)$ approaches to a similar level for these two driving voltages, indicating that with sufficient time the dynamic alignment settles down to the same steady-state alignment configuration.

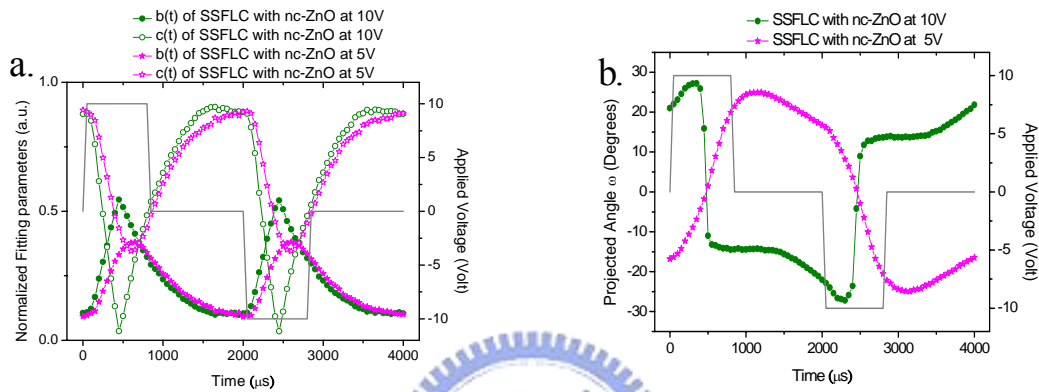


Figure 3-12 Comparing the switching parameters of the nc-ZnO doped SSFLC cell with two different applied voltages. The curve with circle symbols is taken with $\pm 10\text{V}$ and the lines with star symbols is with $\pm 5\text{V}$. (a) Normalized fitting parameters (symbols) of the EO azimuthal patterns and the applied voltage (solid line) as a function of time. (b) The deduced orientation angle of the projected optic axis of SSFLC film are shown. The rubbing direction of the SSFLC cell is set to along 0 degree.

In conclusion, nc-ZnO nanocrystals were successfully used to improve the optical transmission property of a SSFLC cell by 2.27 times at no applied field. When the cell is driven by a pulse of $\pm 10\text{V}$, the switching time of the electro-optical response of the nc-ZnO doped SSFLC cell can be reduced. In addition, an enhanced dynamic alignment with nc-ZnO doping can also be observed. ZnO nanocrystals appear to provide a novel binding effect on FLC molecules and lead to an improved LC alignment quality in both steady-state and dynamic processes.

Chapter 4

Time-Resolved FTIR Spectroscopy of SSFLC with and without nc-ZnO Doping

4.1 Principle of FTIR

Molecules are comprised of atoms, which are connected by chemical bonds. Polyatomic molecules can exhibit periodic vibrational motions [32]. The resulting intra-molecular motions can be expressed as a superposition of so-called normal modes with atoms vibrating with the same phase and normal frequency. Molecules can be excited by photons by taking up a quantized energy $h\nu_s$. Light quanta in the infrared region with a wavelength λ of 2.5 to 1000 μm possess energy of $h\nu = hc\nu'$ with $\nu' = 4000$ to 10 cm^{-1} . A molecule irradiated with a continuous spectrum of infrared radiation may absorb photon with energy $h\nu_s$, hence the spectrum of the remaining radiation shows an absorption dip at the frequency ν_s . This process is demonstrated in the Figure 4-1.

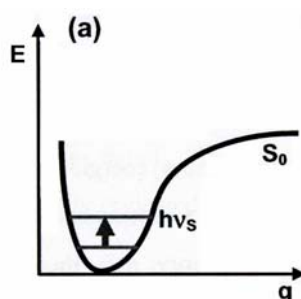


Figure 4-1 The excitation of a vibrational state in the electronic ground state S_0 by infrared absorption.

A molecule with n atoms possesses $k = 3n-6$ normal vibrations. These vibrations may absorb infrared radiation when the infrared causes a modulation in the molecular dipole moment μ_k :

$$\mu_k = \mu_0 + \left(\frac{\partial \mu}{\partial q_k} \right)_0 q_k + \frac{1}{2} \left(\frac{\partial^2 \mu}{\partial q_k^2} \right)_0 q_k^2 + \dots, \quad (4.1)$$

with the k th normal coordinate $q_k = q_k^0 \cdot \cos(2\pi\nu_k t + \varphi_k)$. A molecular vibration is infrared active if the molecular dipole moment can be modulated with the normal mode, *i.e.*,

$$\left(\frac{\partial \mu}{\partial q} \right)_0 \neq 0 \quad . \quad (4.2)$$

Fourier-transform spectroscopy (FTS) has advantages over many other techniques to yield broad spectral range with high resolution [33]. A typical FTS is shown in Figure 4-2.

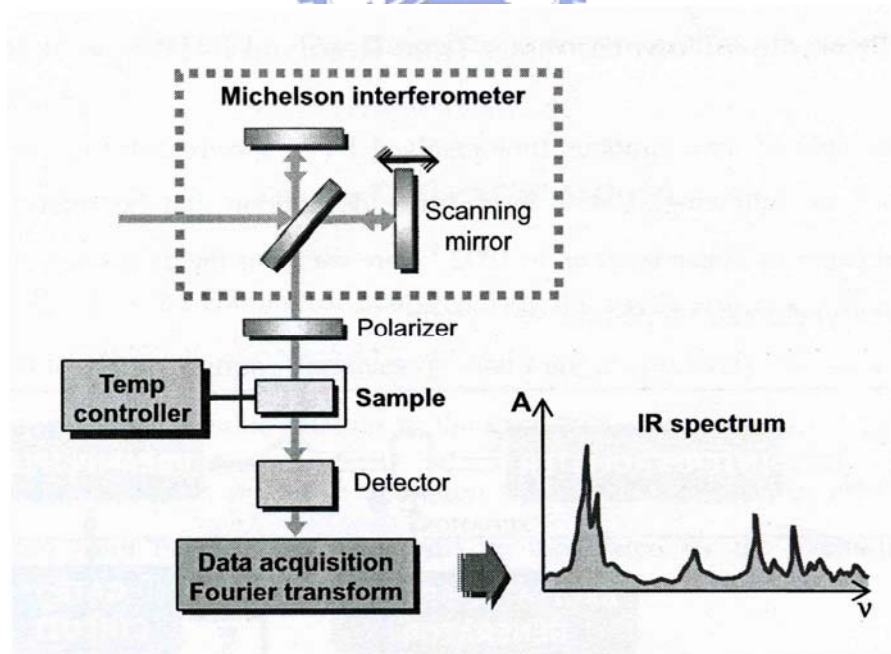


Figure 4-2 Schematic of a FTS system.

The high throughput and multiplex advantage of FTS give signal-to-noise (S/N) improvements over dispersive spectroscopic techniques. In this study, a Fourier-transform infrared (FTIR) spectrometer is used to analyze the molecular motions of SSFLC with and without doping nc-ZnO.

Time-resolved FTIR

In 1992, Masutani *et al.* [34] proposed an asynchronous time-resolving concept with a conventional Fourier-transform infrared (FTIR) spectrometer. The most important feature of this method is that it does not require synchronization between the timing for the time resolving and that for the sampling of the analog-to-digital (A/D) converter. A typical configuration of the time-resolving method is shown in Figure 4-3 [34].

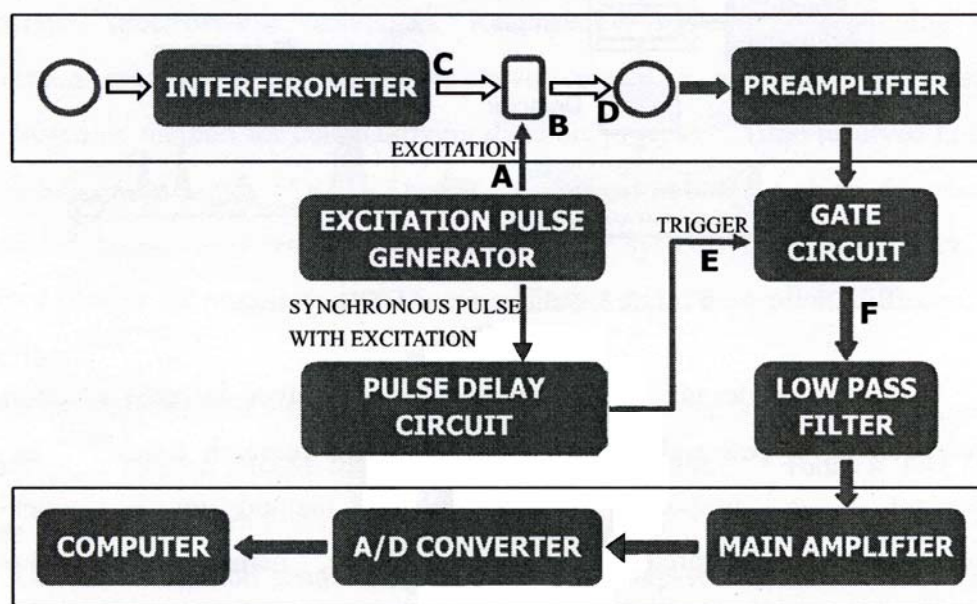


Figure 4-3 Typical setup for the asynchronous time-resolved FTIR. The signal-processing assembly for time-resolved measurement is shown on the middle, while the units constituting a conventional FTIR spectrometer are depicted in the boxes at the top and bottom.

To carry out the time-resolving measurement, a signal-processing assembly (the middle part of Figure 4-3) is attached to a conventional continuous-scan FTIR system. The

components in the assembly include a pulse generator, a pulse delay circuit, a gate circuit and a low-pass filter. Assuming that periodic excitation pulses are generated with a period τ to excite a sample, a periodic response induced by the excitation can be obtained. The transmitted infrared spectrum after the sample can be described by

$$T(\bar{\nu}, t) = T_0(\bar{\nu}) + \Delta T(\bar{\nu}, t) * III_\tau(t), \quad (4.3)$$

where $T_0(\bar{\nu})$ denotes the component unperturbed by the excitation, and $T(\bar{\nu}, t)$ is that changes with the excitation. Variables $\bar{\nu}$ and t are the wave number and time variable relating to the excitation. $III_\tau(t)$ is Dirac delta comb used to represent the repetitive excitation with a period of τ . An interferogram acquired with an interferometer will be modulated by the excitations. This modulated interferogram $F(x, t)$ can be expressed as

$$F(x, t) = \int_{-\infty}^{+\infty} T(\bar{\nu}, t) B(\bar{\nu}) \cos 2\pi x \bar{\nu} d\bar{\nu} = F_0 + \int_{-\infty}^{+\infty} \{T(\bar{\nu}, t) * III_\tau(t)\} B(\bar{\nu}) \cos 2\pi x \bar{\nu} d\bar{\nu} \quad (4.4)$$

with $F_0(x) = \int_{-\infty}^{+\infty} T_0(\bar{\nu}, t) B(\bar{\nu}) \cos 2\pi x \bar{\nu} d\bar{\nu}$,

where $F_0(x)$ is the component of the interferogram unperturbed by the excitation and $B(\bar{\nu})$ is the spectrum of the light source. The trigger pulses generated from a delay circuit are delayed from the leading edge of the excitation pulses by $\Delta\tau$. At a delay time $\Delta\tau$, the modulated signal arriving at the gate circuit is converted into a discrete interferogram of

$$\begin{aligned} F(x, t) &= III_\tau(t - \Delta\tau) \cdot [F_0 + \int_{-\infty}^{+\infty} \{\Delta T(\bar{\nu}, t) * III_\tau(t)\} B(\bar{\nu}) \cos 2\pi x \bar{\nu} d\bar{\nu}] \\ &= III_\tau(t - \Delta\tau) \cdot \int_{-\infty}^{+\infty} T(\bar{\nu}, t) B(\bar{\nu}) \cos 2\pi x \bar{\nu} d\bar{\nu}, \end{aligned} \quad (4.5)$$

where $III_\tau(t - \Delta\tau)$ denotes the gating pulse. A time-resolved continuous interferogram at delay time $\Delta\tau$ can be recovered from the low-pass filter by properly removing the high-frequencies component. The output from low-pass filter can be expressed as

$$F(x, \Delta\tau) = (1/\tau) \int_{-\infty}^{+\infty} T(\bar{\nu}, \Delta\tau) B(\bar{\nu}) \cos 2\pi x \bar{\nu} d\bar{\nu} \quad (4.6)$$

The time-resolved continuous interferograms can be sampled by an A/D converter with a sampling period of τ_0 and is acquired by computer. Inverse Fourier transformation of the digitized interferogram finally gives a time-resolved spectrum at a time delay $\Delta\tau$ from the excitation edge.

4.2 2D IR correlation technique

Generalized two-dimensional infrared (2D-IR) spectroscopy [35,36] is an effective mathematical tool to elucidate spectral details and kinetic sequence of a dynamic system [37]. The perturbation to the dynamic system can be either sinusoidal or of an arbitrary waveform. Generalized 2D correlation is generally presented through synchronous and asynchronous plots. Synchronous 2D spectra are very useful for the determination of the inter- or intramolecular interactions existing in the system of interest, while asynchronous spectra are especially powerful for revealing the anti-correlated variation between the bands. The generalized correlation approach does not require all the data to originate from within a single data set. Therefore it is possible to use the technique to compare experimental data with a reference curve. To construct 2D correlation plot, first we calculate a set of dynamic spectra [38]

$$\tilde{I}(\nu; \Phi, t) = I(\nu; \Phi, t) - \bar{I}(\nu, t) \quad (4.7)$$

from the measured IR absorption spectra $I(\nu; \Phi, t)$ with perturbing parameter Φ . Here t denotes the time delay. The reference spectrum $\bar{I}(\nu, t)$ can be conveniently calculated from

$$\bar{I}(\nu, t) = \frac{1}{2\pi} \int_0^{2\pi} I(\nu; \Phi, t) d\Phi \quad (4.8)$$

We then generate two kinds of 2D correlation spectra, known as synchronous $Syn(\nu_1, t_1; \nu_2, t_2)$ and asynchronous $Asyn(\nu_1, t_1; \nu_2, t_2)$ spectra, from the dynamic spectra

$$\begin{aligned}
C(\nu_1, t_1; \nu_2, t_2) &= \langle \tilde{I}(\nu_1; \Phi, t_1) \tilde{I}(\nu_2; \Phi, t_2) \rangle_{0 \leq \Phi \leq 2\pi} \\
&= \text{Syn}(\nu_1, t_1; \nu_2, t_2) + i \text{Asyn}(\nu_1, t_1; \nu_2, t_2)
\end{aligned} \tag{4.9}$$

The bracket $\langle \dots \rangle_{\Phi}$ denotes a correlation operation, which is defined as

$$\begin{aligned}
\langle \tilde{I}(\nu_1; \Phi, t_1) \tilde{I}(\nu_2; \Phi, t_2) \rangle_{0 \leq \Phi \leq 2\pi} &= \frac{1}{2\pi} \int_0^{2\pi} \tilde{I}(\nu_1; \omega, t_1) \tilde{I}^*(\nu_2; \omega, t_2) d\omega \\
\text{with } \tilde{I}(\nu; \omega, t) &= \int_0^{2\pi} \tilde{I}(\nu; \Phi, t) e^{-i\omega\Phi} d\Phi
\end{aligned} \tag{4.10}$$

However we shall emphasize that the correlation peak height is changed not only with the orientation of IR dipole but also with the spectral intensity of IR absorption peak. Therefore in order to remove the influence of the spectral intensity variations among different IR active modes and retrieve correctly the orientational variation, a global 2D phase map had been developed [37]. The global phase map can be obtained as

$$\Theta(\nu_1, \nu_2) = \arctan \left\{ \text{Asyn}(\nu_1, t_1; \nu_2, t_2) / \text{Syn}(\nu_1, t_1; \nu_2, t_2) \right\} . \tag{4.11}$$

For simplicity, consider a case of two spectral peaks at frequencies of ν_1 and ν_2 with sinusoidal responses of period of T

$$y_1 = a(\nu_1) \cos[2\pi t / T + \theta_1] + b(\nu_1) \tag{4.12}$$

$$y_2 = a(\nu_2) \cos[2\pi t / T + \theta_2] + b(\nu_2), \tag{4.13}$$

where $a(\nu_j)$, t , θ_j and $b(\nu_j)$ are amplitude, time, time lag and offset value of the sinusoidal responses at a given spectral frequency of ν_j respectively. Therefore the synchronous and asynchronous correlation intensities for the sinusoidal systems can be written as [37]

$$\Phi(\nu_1, \nu_2) = \frac{1}{2} a(\nu_1) a(\nu_2) \cos(\theta_1 - \theta_2) \tag{4.14}$$

$$\Psi(\nu_1, \nu_2) = \frac{1}{2} a(\nu_1) a(\nu_2) \sin(\theta_1 - \theta_2) \tag{4.15}$$

The normalized synchronous and asynchronous functions can be used to yield a direct comparison by combining Eqs. (4.14) and (4.15) into a correlation phase angle. In this

way, the effect of $a(\nu_1)$ and $a(\nu_2)$ can be removed and yields an assumed uniform circular motions of response vectors on a complex phase plane derived from the sinusoidal responses in system. The normalized synchronous and asynchronous functions can be calculated as

$$\Phi_n(\nu_1, \nu_2) = \frac{\Phi(\nu_1, \nu_2)}{\frac{1}{2}a(\nu_1)a(\nu_2)} = \cos(\theta_1 - \theta_2) \quad (4.16)$$

$$\Psi_n(\nu_1, \nu_2) = \frac{\Psi(\nu_1, \nu_2)}{\frac{1}{2}a(\nu_1)a(\nu_2)} = \sin(\theta_1 - \theta_2). \quad (4.17)$$

Therefore, the phase difference between the two responses at the frequencies ν_1 and ν_2 can be determined as

$$\Theta(\nu_1, \nu_2) = \arctan \left\{ \frac{\Psi_n(\nu_1, \nu_2)}{\Phi_n(\nu_1, \nu_2)} \right\} = \theta_1 - \theta_2 \quad (4.18)$$

The above result will serve as the ensemble average of the phase delay effect of multiple frequency responses. These methods also can be used to the case for nonperiodic signals which have complicated waveform but the global correlation phase angle no longer has any simple physical meaning such as a fixed time delay.

4.3 FTIR Spectroscopy of SSFLC with and without nc-ZnO doping Infrared absorption spectra and 2D correlation plots in static state

In this section, the SSFLC cell with nc-ZnO doping is prepared by using FELIX 017/100 FLC mixture. The FLC material is prepared by first adding a few drops of nc-ZnO ethanol solution into pure FELIX 017/100 FLC heated to its isotropic phase with vigorous sonication. Then the resulting mixture is put in vacuum to remove the residual ethanol solvent.

Figure 4-4(a) presents the infrared absorption spectra of the SSFLC cells with and without nc-ZnO doping. The IR spectral peaks at 1169, 1250, 1281, 1390.8, 1439, 1514.3, 1584, and 1608 cm^{-1} can be attributed to the normal modes associated with the cores of the effective molecular system; and the peaks at 2857, 2931 and 2957 cm^{-1} to the alkyl chains. The highest-frequency peak at 2957 cm^{-1} is noted to originate from the anti-symmetric CH_3 stretching mode, whereas the two other peaks at 2857 and 2931 cm^{-1} are from the symmetric and anti-symmetric CH_2 stretching along the alkyl chains. The peaks at 1608, 1584, 1514 and 1391 cm^{-1} are mainly from the $\text{C}=\text{C}$ stretching modes of the benzene ring and the 1439- cm^{-1} peak could arise from the $\text{C}=\text{C}$ stretch of pyrimidine ring. The remaining normal modes at 1169 and 1250 (anti-sym) and 1281 cm^{-1} (sym) are associated with the $\text{C}-\text{O}-\text{C}$ stretching modes [39]. In Figure 4-4(b), the synchronous autocorrelation peaks are deduced from the FTIR spectra shown in Figure 4-4(a). It is found that the spectral profiles of the FLC cell doped with nc-ZnO are similar to that of the pure FLC but the peak values of these two cells are different. The detailed analyses will be presented in the following.

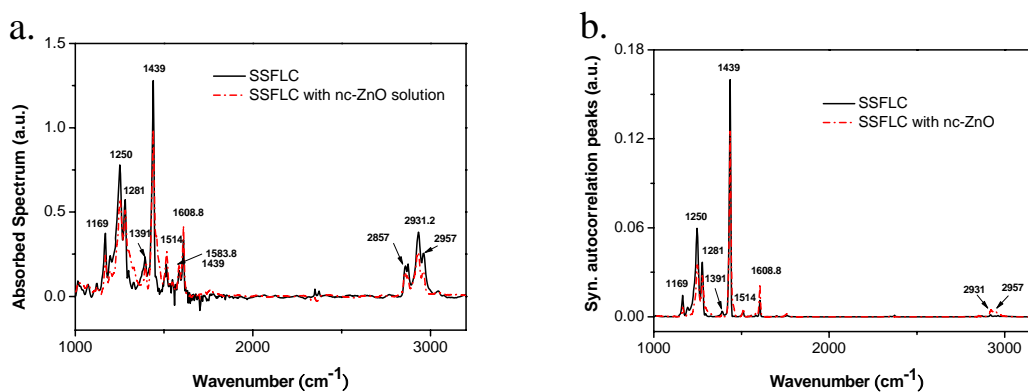


Figure 4-4 (a) FTIR spectra and (b) autocorrelation plots of the SSFLC cells with and without nc-ZnO doping at 30°C.

Figure 4-5(a) shows the FTIR spectra and Figure 4-5(b) the corresponding synchronous autocorrelation peaks of the SSFLC cells with and without nc-ZnO doping

from 1200 to 1650 cm^{-1} . The 2D IR correlation plots deduced from the FTIR spectra reveal that the peaks at 1608, 1584, and 1514 cm^{-1} , which are from the C=C stretching modes of the benzene ring, are larger in the FLC cell doped with nc-ZnO than those in the pure FLC cell, while the peaks at 1391 cm^{-1} (the C=C stretching mode of the benzene ring), 1439- cm^{-1} (the C=C stretching modes of pyrimidine ring), 1250 (anti-sym) and 1281 cm^{-1} modes (sym. C–O–C motion) of the FLC cell doped with nc-ZnO are smaller than those of the pure FLC. The peak positions of 1250, 1281, 1391 and 1514 cm^{-1} show a spectral shift of about 1-2 cm^{-1} with nc-ZnO doping

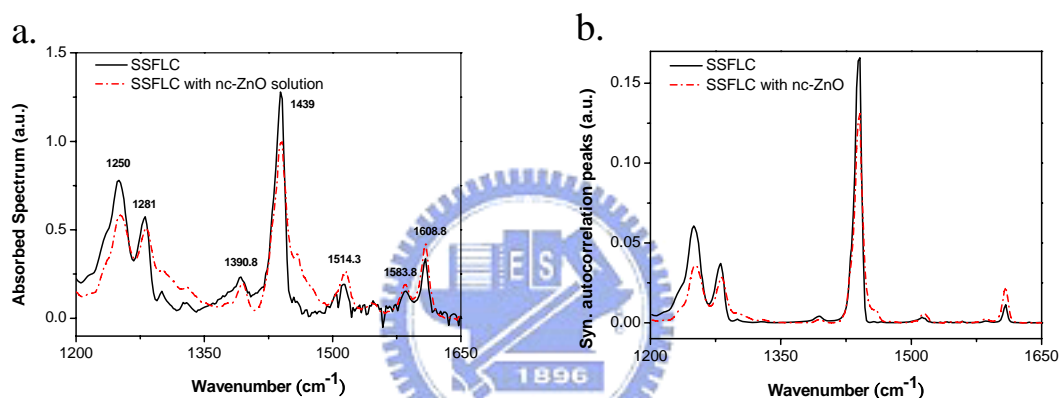


Figure 4-5 FTIR spectra and (b) autocorrelation plots of the SSFLC cells with and without nc-ZnO doping in the region of 1200 to 1650 cm^{-1} measured at 30°C.

Figure 4-6(a) shows the FTIR spectra from 2800 to 3100 cm^{-1} and Figure 4-6(b) the corresponding synchronous autocorrelation peaks of the SSFLC cells with and without nc-ZnO doping. In the spectral range, the observed FTIR spectral peaks of the pure FLC are larger than that of the FLC with nc-ZnO doping (Figure 4-6(a)). By using 2D IR correlation technique, the synchronous autocorrelation peaks of the nc-ZnO doped SSFLC cell are higher than that of pure SSFLC cell. The 2D correlation peaks at 2931 (the anti-symmetric CH_2 stretching) and 2957 cm^{-1} (anti-symmetric CH_3 stretching mode) of the SSFLC cell doped with nc-ZnO are four times large than those of the pure FLC. Furthermore the 2D correlation peak positions at 2857 and 2957 cm^{-1}

exhibit clear frequency shift from those of pure SSFLC, indicating an improved spectral resolution with 2D correlation technique.

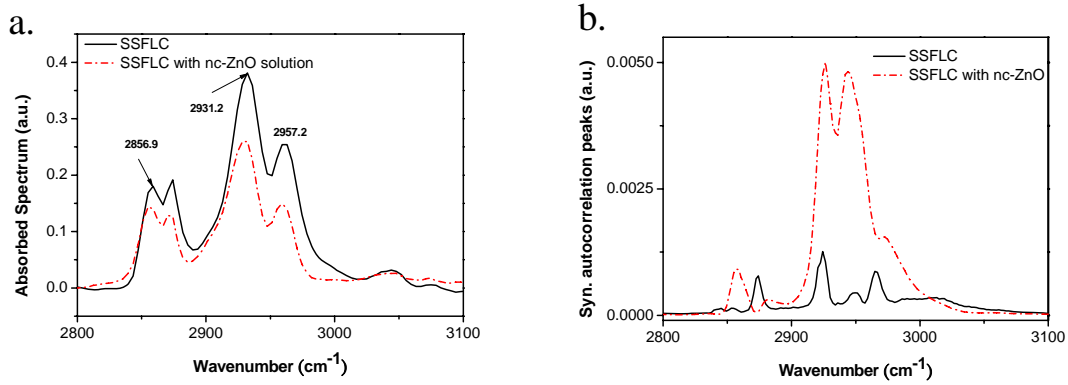


Figure 4-6 FTIR spectra and (b) autocorrelation plots of the SSFLC cells with and without nc-ZnO doping in the region of 2800 to 3100 cm^{-1} measured at 30°C.

Angular pattern of polarization-angle dependent IR absorption peak

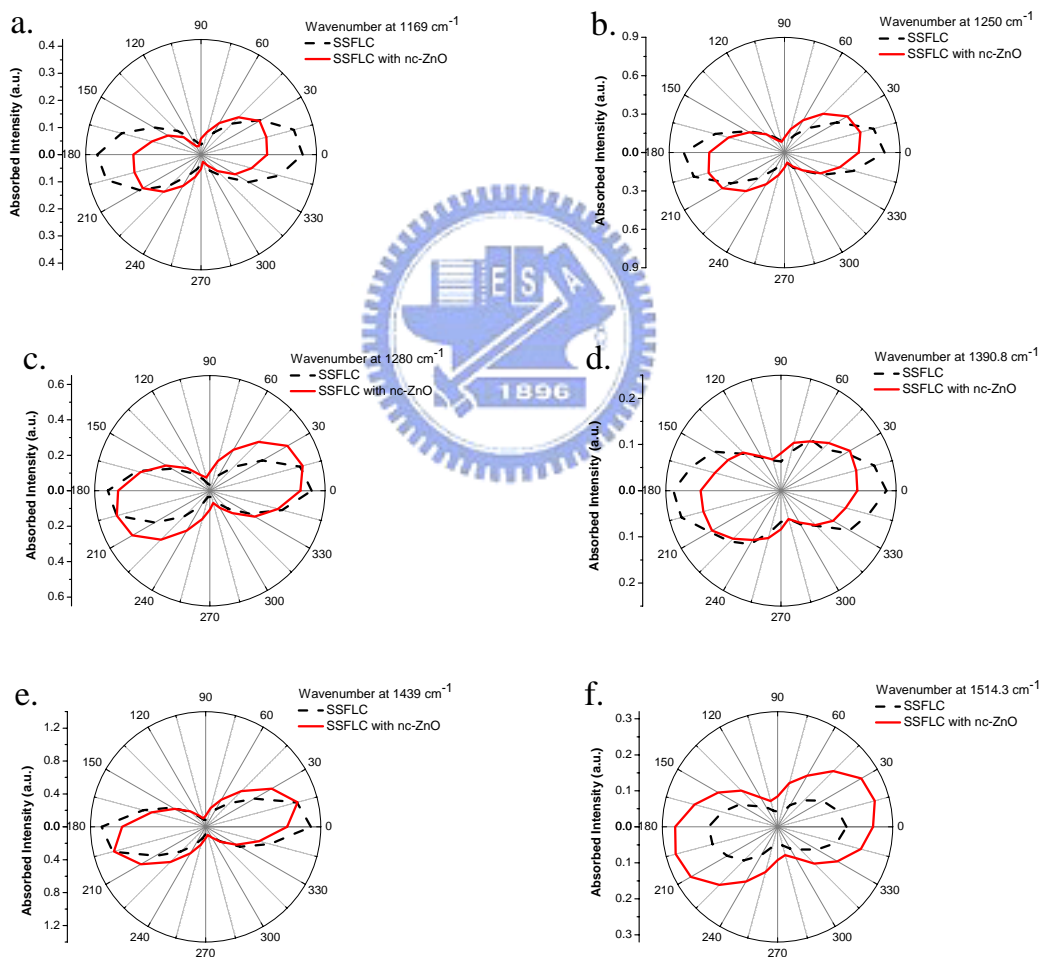
Two parameters, which can be deduced from polarization-angle dependence of IR absorption $A(\Phi)$, are used to portray the orientation and uniaxial alignment of a molecular segment. For normal incidence, $A(\Phi)$ can be expressed as

$$A(\Phi) = A_0 + U \cdot \cos^2(\Phi - \Phi_0) \quad (4.7)$$

where A_0 and U represent the orientation-independent term and the aligned component of an atomic group, Φ denotes the angle between the incident infrared polarization and the rubbing direction of the cell substrates, and Φ_0 represents the apparent angle of the IR dipole projected onto the substrate surface.

Figure 4-7 shows the FTIR angular patterns of some IR active modes at 1169, 1250, 1281, 1391, 1439, 1514, 1584, and 1608 cm^{-1} taken from the SSFLC cells with and without nc-ZnO doping. From this figure, the apparent angles of these IR dipole moments of the pure FLC cell were found to locate at about 5 degrees but those of the SSFLC cell with nc-ZnO doping were found to rotate to about 15 degrees. The IR peak

intensities at 1514 cm^{-1} (f) 1584 cm^{-1} (g) 1608 cm^{-1} (h) of the FLC cell doped with nc-ZnO are larger than which of the pure FLC. Interestingly, the dichroic ratios of the SSFLC with nc-ZnO doping are much higher than those of the pure FLC, while the peaks at 1169(a), 1250(b), 1281(c), 1390.8(d) and 1439- cm^{-1} (e) of the doped SSFLC cell are smaller than those of the pure FLC cell. We attribute these differences are mainly due to that the ZnO nanocrystals affect the alignment configuration of the FLC molecules and reflect an orientation change of IR dipole moment to about 10 degrees, and an intensity enhancement of the C=C stretching modes of benzene ring.



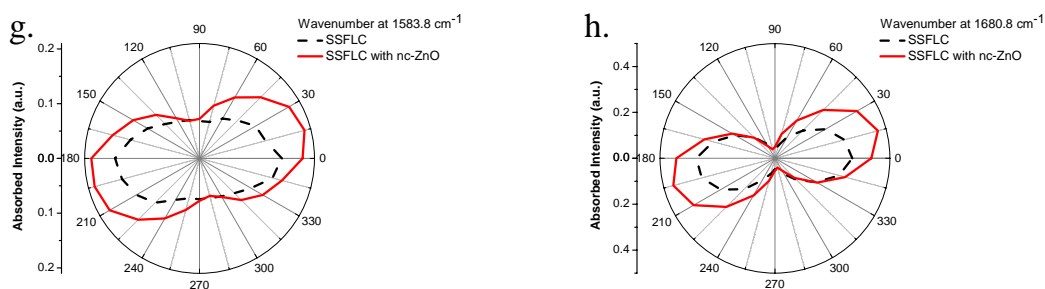


Figure 4-7 FTIR angular patterns of some IR active modes at (a) 1169 cm^{-1} (b) 1250 cm^{-1} (c) 1281 cm^{-1} (d) 1391 cm^{-1} (e) 1439 cm^{-1} (f) 1514 cm^{-1} (g) 1584 cm^{-1} (h) 1608 cm^{-1} measured on the SSFLC cells with and without nc-ZnO doping at 30°C .

Figure 4-8 presents the IR dipole moment of the SSFLC cells with and without nc-ZnO doping at 2857 , 2931 and 2957 cm^{-1} . The observed azimuthal patterns of the IR peaks of the FLC with nc-ZnO doping are perpendicular to the direction of other IR bands associated to the cores shown in Figure 4-7. However, the azimuthal patterns of the IR peaks of the pure FLC cell show nearly isotropic. This is the strong evidence to support that nc-ZnO dopant can modify the alignments of the FLC molecules.

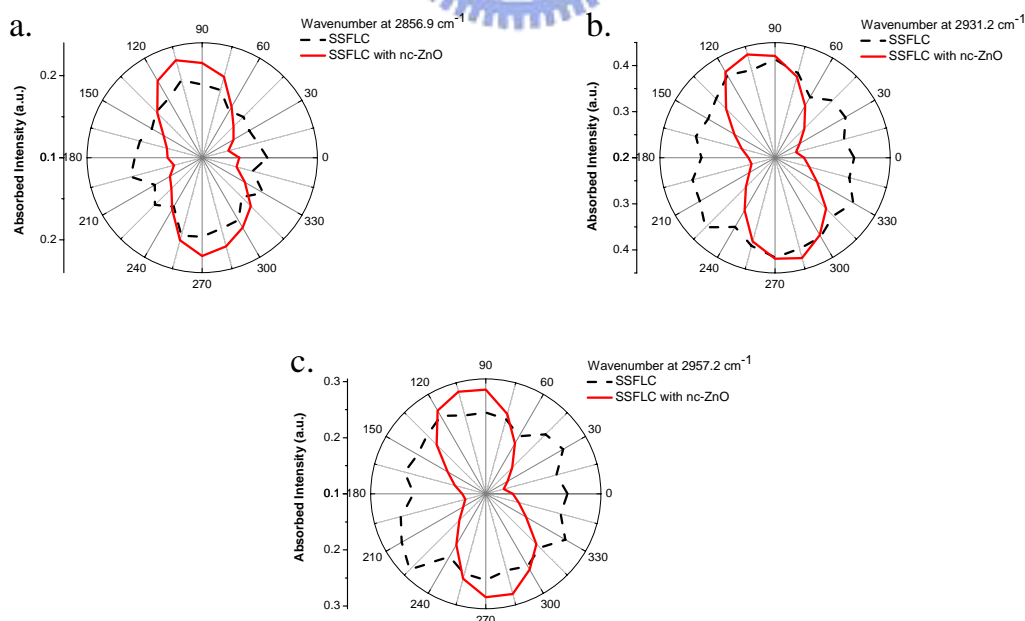


Figure 4-8 FTIR angular patterns of some IR active modes at (a) 2857 cm^{-1} (b) 2931 cm^{-1} (c) 2957 cm^{-1} measured on the SSFLC cells with and without nc-ZnO doping at 30°C .

4.4 trFTIR of SSFLC with and without nc-ZnO doping

Time-resolved polarized FTIR spectra

We had successfully acquired a set of time-resolved polarization-dependent FTIR spectra of the electro-optical switching SSFLC. These spectra were used to deduce the time-resolved polarization angle dependent patterns of the observed IR peaks. The averaged apparent angles of the IR dipoles investigated and the corresponding dichroic ratios can be determined. Figure 4-9 presents the time courses of the apparent angles of the IR dipoles vary with the external electric field at various delay time. The filled symbols indicate the pure SSFLC and the opened symbols show the results of the nc-ZnO doped SSFLC cell. For the peak at 1439 cm^{-1} (red-line) arising from the C=C stretch of pyrimidine ring, during the positive driving cycle the IR dipole rotates about 25 degrees in the pure SSFLC cell but it changes only 15 degrees in the nc-ZnO doped SSFLC cell. Therefore, the period of the driving field is too short to allow FLC molecules reaching their final orientation. The similar results were found at 1252 (blue-line) and 1606 cm^{-1} (green-line).

During the field-on, the increasing slopes of the IR dipoles in the SSFLC cell are large than that of the SSFLC with nc-ZnO doping. The SSFLC cell with nc-ZnO doping cell may have ethanol residue, which can interact with FLC molecules via hydrogen bonding. Thus the nc-ZnO doped FLC shall exhibits a significant increase in viscosity. Indeed, the viscosity of the nc-ZnO doped FLC with ethanol as the spreading solvent increases by 30% (see Table 4-1). Therefore, the IR dipoles in FLC doped with nc-ZnO rotate more slowly than that in pure FLC.

Table 4-1 Comparison of the spontaneous polarization and viscosity of the pure FLC (left), FLC with ethanol residue (add a few drops of ethanol and then dried in vacuum for 8 hours, middle) and FLC doped with 1.28% nc-ZnO (add a few drops of nc-ZnO ethanol solution and then dried in vacuum for 8 hours, left).

	Pure FLC 017		FLC 017 with ethanol residue		FLC 017 doped 1.28% ZnO in ethanol	
	P_s	Viscosity	P_s	Viscosity	P_s	Viscosity
25°C	48.2 nC/cm ²	592.77 mP · S	34.403 nC/cm ²	825.93 mP · S	29.77 nC/cm ²	737.15 mP · S
30°C	46.74 nC/cm ²	483.45 mP · S	32.78 nC/cm ²	539.37 mP · S	27.89 nC/cm ²	637.73 mP · S
40°C	43.50 nC/cm ²	412.27 mP · S	26.59 nC/cm ²	275.73 mP · S	24.295 nC/cm ²	455.125 mP · S

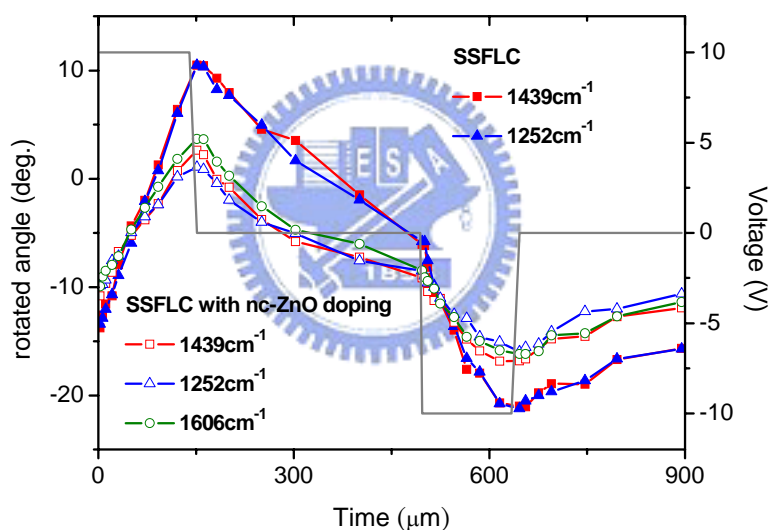


Figure 4-9 The dynamic curve of the averaged apparent angles of IR dipoles associated with the cores of the SSFLC cells with and without nc-ZnO doping measured at 30°C. The waveform of the bipolar driving pulses is included for comparison.

The synchronous correlation of the C-O-C stretching mode at 1252 cm⁻¹ of the SSFLC and the SSFLC with nc-ZnO doping reaches a peak at $t=50 \mu\text{sec}$ and $t=70 \mu\text{sec}$, respectively, after the rising edge of the positive applied field (see Figure 4-10). At the beginning of the applied field the FLC molecules were aligned dynamically. During the

field-off period, the SSFLC with nc-ZnO doping exhibits a higher correlation than that of SSFLC. When the negative field is applied, the synchronous correlation of the two cells both decrease continuously with the correlation in the nc-ZnO doped SSFLC cell higher than pure FLC.

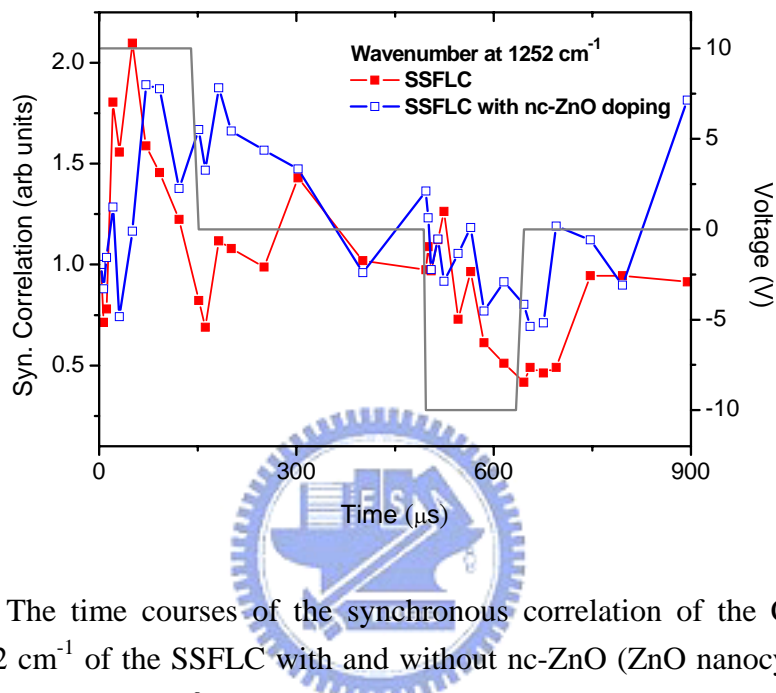


Figure 4-10 The time courses of the synchronous correlation of the C-O-C stretch mode at 1252 cm^{-1} of the SSFLC with and without nc-ZnO (ZnO nanocrystal solution) doping cells measured at 30°C . The waveform of the bipolar driving pulses is included for reference.

Time-resolved 2D IR correlation analysis of the switching dynamics of the FLC mixture

The switching dynamics of an SSFLC can be better understood by monitoring the field-induced reorientation of different molecular segments. The time-resolved polarization angle-dependent patterns of infrared absorption peaks are subject to 2D correlation analyses and the time courses of the synchronous and the asynchronous peaks are yielded. Time courses of 2D IR correlation phase angle derived by Eq. (4-11) are shown in Figure 4-11(a) for the pure SSFLC cell and Figure 4-11(b) for the SSFLC with nc-ZnO doping. It can be found that the correlation phase angles of the SSFLC

(Figure 4-11(a)) are divided into four groups – (1) 1250 (anti-sym) and 1281 cm^{-1} (sym) associated with the C–O–C stretching modes; (2) 1439- cm^{-1} arisen from the C=C stretch of pyrimidine ring; (3) 1584 and 1608.8 cm^{-1} mainly from the C=C stretching modes of the benzene ring; (4) 2931.2 cm^{-1} from the anti-symmetric CH_2 stretching along the alkyl chains. We can calculate the phase differences between the different molecular segments. The temporal profiles of the correlation phase angles reflect the orientation variations of the IR dipoles. During the positive driving cycle from 0 to 500 μsec , in which the correlation phase angle rotates 40 degrees, the groups (1), (2) and (3) keep constant for the phase differences among the sub molecular groups shown. The group (4) of 2931.2 cm^{-1} behaves more randomly than the other three groups.

In Figure 4-11(b), we found that the correlation phase angle of the molecular groups of FLC doped with nc-ZnO mainly separate into two groups—core groups and alkyl-chain groups. The core groups of FLC with nc-ZnO doping include 1250 (anti-sym) and 1281 cm^{-1} (sym) associated with the C–O–C stretching modes; 1439- cm^{-1} arising from the C=C stretch of pyrimidine ring; 1584 and 1608.8 cm^{-1} mainly from the C=C stretching modes of the benzene ring. Except to 1584 cm^{-1} , these core groups appear to tie together during the positive or negative field-on and field-off periods. In the positive period, the correlation phase angles of the core groups change about 30 degrees; while during the negative driving period, they change only about 20 degrees. The total correlation phase angles of SSFLC with nc-ZnO doping are about 10 degrees smaller than that of SSFLC. Because ethanol, which was used to disperse ZnO nanoparticles into FLC, cannot be completely removed from FLC material. Thus the nc-ZnO doped FLC has an increased viscosity and decreased spontaneous polarization compared to the pure FLC material. This causes slower field-induced reorientation speed and smaller rotation angle in a fixed driving period for the core groups. The alkyl chain groups consist of 2957 cm^{-1} , originated from the anti-symmetric CH_3 stretching

mode, and the two other peaks at 2857 and 2931 cm^{-1} , which are from the symmetric and anti-symmetric CH_2 stretching along the alkyl chains. FLC with nc-ZnO doping exhibits an enhanced alignment of these alkyl chain groups. All of these studies support that the ZnO nanocrystals affect the static and dynamic behavior of FLC.

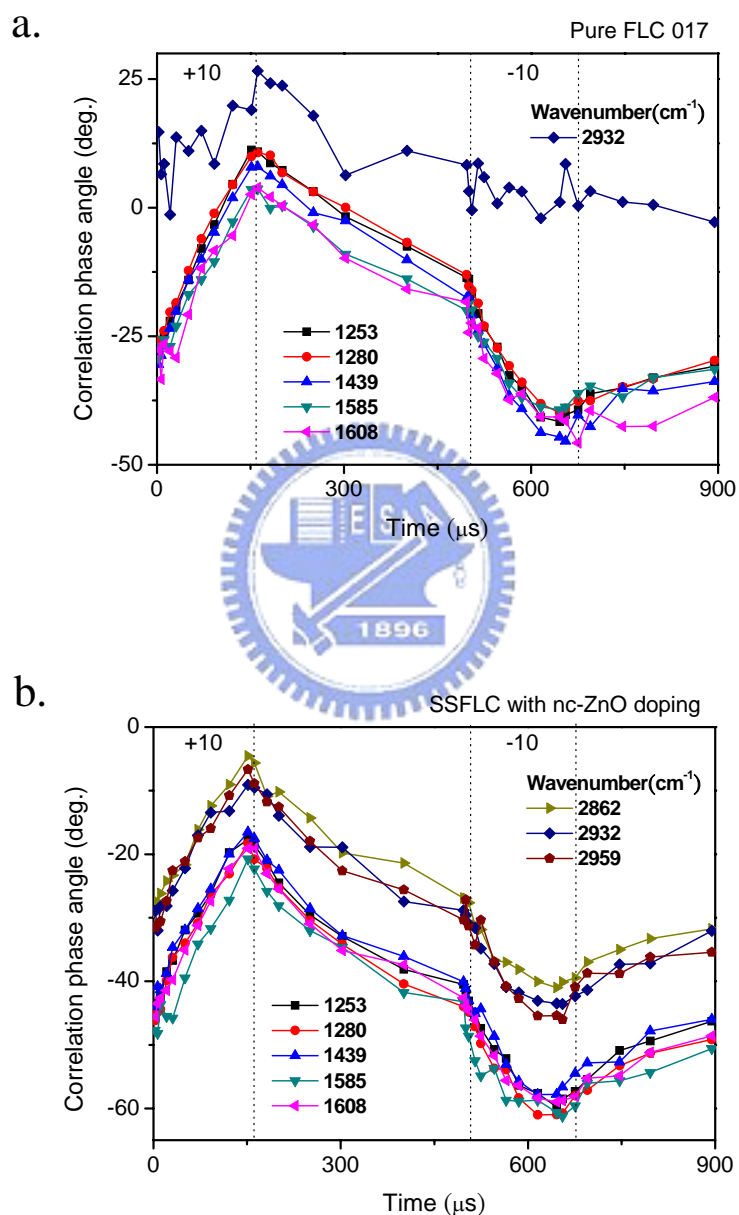


Figure 4-11 Time courses of 2D IR correlation phase angle generated from the time-resolved polarization-angle dependent spectrum of (a) SSFLC and (b) SSFLC with nc-ZnO doping cells measured at 30 $^{\circ}\text{C}$.

Chapter 5

Conclusions and Future Prospect

In conclusion of this study, molecular alignment and electrical properties of surface-stabilized ferroelectric liquid crystal (SSFLC) with and without doping of ZnO nanocrystals (nc-ZnO), we demonstrate that

- (1) The nc-ZnO doping improves the azimuthal alignment of FLC and results in a narrower distribution.
- (2) The nc-ZnO doping also improves the polar distribution of FLC director by effectively reducing the FWHM width.
- (3) By using the equivalent electronic circuit, both the SSFLC cells with and without nc-ZnO doping exhibit symmetric CV hysteretic curves with respect to 0V and the FLC doped with ZnO nanocrystals exhibits a lower coercive voltage.
- (4) The dipoles of the ZnO nanocrystal can effectively tie up the surrounding FLC species to perform a collective switching under an external driving field.
- (5) The nc-ZnO nanocrystals were successfully used to improve the optical transmission property of a SSFLC cell by 2.27 times at no applied field.
- (6) The switching time of the electro-optical response of the nc-ZnO doped SSFLC cell can be reduced by 0.5 times.
- (7) ZnO nanocrystals provide a novel binding effect on FLC molecules and lead to an improved LC alignment quality in both steady-state and dynamic processes.

Some works remain to be done in the future:

- (1) Besides to study on the material of FLC, the same experimental and analyzed methods can be used for other LC material, such as nematic LC or AFLC.
- (2) To change the concentration of nc-ZnO doping and to research the accompanying variation of the optical and electrical properties of LC material.
- (3) Use nc-ZnO doped with other magnetic material, such as Mn or Co, to enhance the alignment of FLC molecules.
- (4) Using different spectroscopic measurement, like raman scattering spectroscopy or second harmonic generator etc., to analyze the dynamic behavior of the FLC molecule doped with nc-ZnO.



Reference

- [1] P. J. Collings, *Liquid Crystals* (IOP Publishing Ltd, 1990).
- [2] P. J. Collings and M. Hird, *Introduction to Liquid Crystals: Chemistry and Physics* (CRC Press, London, 1997).
- [3] D. Demus, J. W. goodby, G. W. Gray, H. W. Spiess and V. Vill, *handbook of Liquid Crystals* (Wiley-VCH, Weinheim, 1998)
- [4] R. B. Meyer, C. L. Yang, *Appl. Phys. Lett.*, 80, 3721 (2002).
- [5] Pochi Yeh and Claire Gu, *Opticas of Liquid Crystal Display* (John Wiley and Sons, Inc., 1999).
- [6] N.A Clark and S.T. Lagerwall, *Appl. Phys. Lett*, 36, 899 (1980)
- [7] I. musevic, R. Blinc and B. Zeks, *The physics of Ferroelctric and Antiferroelectric liquid crystals* (World Scientific, 2000), p157-183.
- [8] D. J. Goyal, C. Agashe, M. G. Takwale, V. G. Bhide, S. Mahamuni, and S. K. Kulkarni, *J. Mater. Res.*, 8, 1052 (1993).
- [9] Chin-hsien Hung, *Synthesis and Characterization of ZnO Nanorods, Nanotips Arrays and Nanohybrid Films* (Chiao Tung University, Hsinchu, 2004), p.75.
- [10] Eric A. Meulenkaamp, *J. Phys. Chem. B*, 102 (29), 5566 (1998).
- [11] L. Spanhel and M. A. Anderson, *J. AM. Chem. Soc.*, 113, 2826 (1991).
- [12] S. Monticone, R. Tufeu and A. V. Kanaev, *J. Phys. Chem. B*, 102, 2854 (1998).
- [13] Chien Li Lee and Jung Y. Huang, *An Imaging Polarimetic Technique for Measuring both the Thickness and Optic-axis of a Uniaxial Film* (Chiao Tung University, Hsinchu, 2004), p.7.
- [14] Yoshio Nishida and Masanobu Yamanaka, *Review of Scientific Instruments*, 72, 2387 (2001).

- [15] D. S. Kliger, J. w. Lewis, and C. E. Randall, *Polarized Light in Optics and Spectroscopy* (Academic Press, San Diego, CA, 1990), p.75.
- [16] T. J. Scheffer and J. Nehring, *J. Appl. Phys.*, 48, 1783 (1977).
- [17] J. Funfschilling and M. Schadt. *Jap. J. Appl. Phys.*, 33, 4950 (1994).
- [18] T. Yamaguchi, Y. Hara, H. Fujiwara, G.Itoh and H. Okumura, *Jap. J. Appl. Phys.*, 38, 4127 (1999).
- [19] L. M. Blinov, E. P. Pozhidzev and F. V. Podgornov, S. A. Pikin, S. P. Palto, a. Sinha, A. Yasuda, S. Hashimoto and W.Haase, *Phys. Rev. E*, 66, 021701 (2002).
- [20] I. D. Mayergoyz, *Mathematical Models of Hysteresis* (Springer, New York, 1991).
- [21] A. T. Bartic, D. J. Wouters, H. E. Maes, J. T. Rickes and R. M. Waser, *J. Appl. Phys.*, 89, 3420 (2001).
- [22] H. Goebel, M. Ullmann, G. Schindler, and M. Kastner, *International Conference on Solid State Devices and Materials* (1999), p.386
- [23] J. T. Evans and J. A. Bullington, *IEEE 7th International Symposium on Applications of Ferroelectrics* (New York, 1991), p692.
- [24] M. Rahman, S. K. Kundu and B. K. Chaudhuri, *J. Appl. Phys.*, 98, 024114 (2005).
- [25] L. M. Blinov and V. G. Chigrinov, *Electrooptic Effects in Liquid Crystal Materials* (Springer, New York, 1994), p380.
- [26] S. L. Miller, J. R. Schwank, R. D. Nasby and M. s. Rodgers, *J. Appl. Phys.*, 70, 2849 (1991).
- [27] G. Arfken, *Mathematical Methods for Physicists* (Academic, New York, 1970)
- [28] P. Yang, D. L. Carroll, J. Ballato and R. w. Schwartz, *Appl. Phys. Lett.*, 81, 4583 (2002).
- [29] C.Reynaerts and A. De Vos, *J. Phys. D*, 22,1504 (1989).

- [30] N. Itoh, M. Koden, S. Miyoshi and T. Akahane, *Liq. Cryst.*, 18, 109 (1995).
- [31] A. Jiang, M. Dawber, J. F. Scott, C. Wang, P. Migliorato, and M. Gregg, *Jpn. J. Appl. Phys.*, Part1 42, 6982(2003).
- [32] B. Schrader and D. Bougeard, *Infrared and Raman Spectroscopy: Methods and Applications* (Willey-VCH, Weinheim, 1995).
- [33] L. T. Letendre, H. L. Dai, I. A. McLaren and T. J. Johnson, *Rev. Sci. Instrum.*, 70, 18 (1999).
- [34] K. Masutani, H. Sugisawa, A. Yokota, Y. Furukawa and M. Tasumi, *Appl. Spectrosc.*, 46, 560 (1992).
- [35] I. Noda, *Appl. Spectrosc.*, 44, 550 (1990).
- [36] I. Noda, *Appl. Spectrosc.* 47, 1329 (1993)
- [37] I. Noda and Y. Ozaki, *Two-Dimensional Correlation Spectroscopy-Applications in Vibrational and Optical Spectroscopy*, (Willey-VCH, Weinheim, 2004).
- [38] Shih W. T., Huang J. Y., and Zhang J. Y., *Liq. Cryst.* , 31, 377 (2004).
- [39] Zhao J G, Yoshihara T, Siesler H W and Ozaki Y, *Phys. Rev. E*, 64, 31704(2001).